RESEARCH ARTICLE | OCTOBER 29 2024

Multiscale analysis of Reynolds stresses and its dissipation rates for premixed flame–wall interaction

Sanjeev Kumar Ghai ; Umair Ahmed ; Nilanjan Chakraborty ; Markus Klein

Physics of Fluids 36, 105199 (2024)
https://doi.org/10.1063/5.0232629

Physics of Fluids ARTICLE pubs.aip.org/aip/pof

Multiscale analysis of Reynolds stresses and its dissipation rates for premixed flame–wall interaction

Cite as: Phys. Fluids **36**, 105199 (2024); doi: 10.1063/5.0232629
Submitted: 9 August 2024 · Accepted: 7 October 2024 ·
Published Online: 29 October 2024

Sanjeev Kumar Ghai,[1,2] Umair Ahmed,[1] Nilanjan Chakraborty,[1] and Markus Klein[3,a)]

AFFILIATIONS

[1]School of Engineering, Newcastle University, Newcastle-Upon-Tyne NE1 7RU, United Kingdom
[2]Department of Engineering, University of Cambridge, Cambridge CB21PZ, United Kingdom
[3]Department of Aerospace Engineering, University of the Bundeswehr, Munich, 85577 Neubiberg, Germany

[a)]**Author to whom correspondence should be addressed:** markus.klein@unibw.de

ABSTRACT

Direct numerical simulation (DNS) data of flame–wall interaction (FWI) has been utilized to analyze the multiscale nature of turbulent Reynolds stresses and dissipation rate tensor anisotropies within turbulent reacting flow boundary layers across a broad range of scales. The DNS data of head-on quenching of premixed flames propagating through turbulent boundary layers, representative of friction Reynolds numbers Re_τ of 110 and 180, has been explicitly filtered using both two- and three-dimensional Gaussian filter kernels for the purpose of multiscale analysis. The low-pass filter results demonstrate the transition from a 2-component limit to a 1-component limit near the wall with increasing filter width, accompanied by a decrease in isotropy, suggesting a significant alteration in dominant flow patterns and a diminishing tendency toward isotropy. The high-pass filter results indicate a progressive increase in anisotropy with the progress of FWI at the channel center, emphasizing the anisotropy of the large scales with the progress of FWI. Furthermore, behaviors of the second and third invariants of the Reynolds stress tensor remain qualitatively similar to that of the dissipation rate tensor at all stages of FWI, suggesting a link between viscous dissipation and Reynolds stress distributions; notably, there is a stronger isotropic tendency in the dissipation rate tensor when the flame is away from the wall, intensifying with an increase in Reynolds numbers. However, as FWI progresses, the shift in the trend toward the 1-component limit indicates an increase in anisotropy within the turbulent reacting flow for the region near the center of the channel.

I. INTRODUCTION

In wall-bounded turbulent reacting flows, turbulent boundary layers represent a critical zone where the intricate interplay between fluid dynamics and combustion processes profoundly influences heat transfer, pollutant formation, and overall combustion efficiency.[1] Flame–wall interaction (FWI) under turbulent conditions represents a complex three-way interaction between flame, wall, and turbulence. For example, on the one hand, turbulence wrinkles the flame and affects the wall shear stress, whereas the flame affects the turbulence by thermal expansion effects (and change of thermophysical properties) and heats the wall. On the other hand, the wall introduces shear and wall heat loss which gives rise to flame quenching. All of these interlinked processes in FWI are characterized by intricate spatiotemporal dynamics and multiscale interactions. Understanding and quantifying these phenomena is of paramount importance for a wide range of practical applications, including automotive engines, gas turbines, and combustion-based power generation systems.[2] Despite considerable progress in recent years on the understanding of turbulent boundary layers and turbulent reacting flows, the mechanisms governing turbulence–flame–wall interactions remain a challenge due to the inherently nonlinear and multiscale nature of the flame–wall interaction process. In this context, the analysis of Reynolds stress tensor and its dissipation rate tensor emerges as a pivotal avenue for unraveling the intricate dynamics at play, providing valuable insights into the underlying mechanisms governing heat and mass transfer, as well as informing the design of more efficient and environmentally sustainable combustion systems.

Kolmogorov's seminal hypothesis postulated that at sufficiently high Reynolds numbers, small-scale turbulent motions exhibit statistical isotropy, an idea pivotal to turbulence theories.[3] This concept has profound implications for turbulence modeling approaches, distinguishing between methodologies like large eddy simulation (LES) and Reynolds-averaged Navier–Stokes (RANS) simulations. While LES focuses on resolving large turbulent scales and modeling the smaller ones, RANS methodology necessitates modeling the entire energy spectrum, leading to complex constitutive equations. The isotropic assumption for small-scale phenomena in turbulence models, particularly for dissipation tensors, has been a subject of scrutiny, with alternative models proposed to account for non-isotropic turbulent dissipation rates.[4] Recent research has delved into the complex interplay between small-scale turbulence and dissipation mechanisms, revealing persistent anisotropy at local scales.[5] The study of small-scale turbulence physics, closely linked with dissipation mechanisms, has been an area of active research over several decades, as evidenced by seminal works, such as those by Sreenivasan and Antonia.[6] Shen and Warhaft[7] have shown, in turbulent shear flows up to a Taylor-scale Reynolds number of $Re_\lambda = 1000$, that the assumption of local isotropy is not strictly valid at both dissipation and inertial scales, suggesting its improbability even at higher Reynolds numbers. Furthermore, Liu and Pletcher[8] examined the multiscale behavior of anisotropy in turbulent boundary layers, finding that anisotropy persists rather than decays as scales decrease. Klein *et al.*[9] investigated the impact of bubbles on turbulence characteristics in channel flows, revealing anisotropy persisting down to the smallest scales of motion, with significant implications for turbulence modeling approaches. Through a multiscale analysis using a direct numerical simulation (DNS) database of statistically planar turbulent premixed flames, Klein *et al.*[5] highlighted that the heat release induces significant anisotropies, affecting both fluctuation strengths and the characteristic size of structures associated with different velocity components, which have serious implications for turbulence modeling. It is important from a modeling and engineering point of view to understand the roles of different scales involved during the FWI process within turbulent boundary layers, as the vortex stretching phenomenon in turbulence is affected by different scales.[10] Computational fluid dynamics (CFD) relies on a multitude of methods ranging from Reynolds-averaged to large eddy simulation techniques, and they address different ranges of scales of the turbulence kinetic energy spectrum. In the case of FWI, it has been shown in the literature that the small scales of turbulence do not contribute to the straining of the flame when the flame is away from the wall, but the contribution of the small scales of turbulence significantly increases when the flame starts to interact with the wall.[11] To date, no information is available about the behavior of Reynolds stress and viscous dissipation tensors at different scales in the case of FWI. In the present work, DNS data have been used to investigate the behavior of Reynolds stresses and viscous dissipation rate tensors at multiple scales for head-on quenching (HOQ) of premixed flames propagating across a turbulent boundary layer at two different friction Reynolds numbers, $Re_\tau = 110$ and 180. In this regard, the main objectives of this study are:

1. To undertake a comprehensive multiscale analysis of the anisotropies of turbulent Reynolds stress and dissipation tensors across a wide spectrum of filter sizes.
2. To discern and contrast the levels of anisotropy exhibited at various distances from the wall and under different friction Reynolds numbers.
3. To provide in-depth and rigorous physical explanations for the observed phenomena, thereby contributing to the broader understanding of premixed FWI within turbulent boundary layers.

This study aims to advance the fundamental understanding of FWI processes and to provide new insights that can inform the development of enhanced modeling approaches and engineering strategies for turbulent combustion systems. The subsequent sections of this paper are organized as follows: Section II delineates the DNS database utilized for this analysis, along with a comprehensive description of the numerical methods employed in the DNS framework. Section III provides the necessary mathematical background essential for the subsequent analysis. In Sec. IV, results are presented and subsequently discussed. Finally, the concluding section encapsulates the main findings derived from this study, thereby offering valuable insights into the implications and significance of this research.

II. DNS DATABASE

For the present analysis, simulations are conducted using a three-dimensional compressible DNS code known as SENGA+.[12] Spatial derivatives in SENGA+ are computed using a tenth-order finite difference central scheme for internal grid points and the order of accuracy gradually reduces to one-sided second order at non-periodic boundaries. It is worth noting that the decrease in the order of numerical differentiation is only limited to five grid points next to the wall, which fall into the viscous sublayer for the cases considered here. Temporal advancement is achieved by employing an explicit third order low storage Runge–Kutta scheme. A similar numerical approach involving a compressible DNS code was adopted in previous studies of flame–wall interaction (e.g., Ref. 2).

The combustion kinetics are represented through a modified single-step Arrhenius-type chemical mechanism,[13] where the heat of combustion and the activation energy are taken to be functions of the equivalence ratio. It was demonstrated in several previous studies[13,14] that this chemical mechanism captures the experimental results for the variation of laminar burning velocity for hydrocarbon-air combustion. The chemical reaction considered by the present analysis is characterized by

$$1 \text{ unit mass of fuel} + s \text{ unit mass of } O_2 + 3.29s \text{ unit mass of } N_2 \rightarrow (1 + 4.29s) \text{ unit mass of products} \quad (1)$$

where s denotes the stoichiometric oxygen-to-fuel mass ratio. Specifically, methane, CH_4, serves as the fuel, oxygen, O_2, as the oxidizer, and the resulting products consist of water vapor, H_2O, carbon dioxide, CO_2, and nitrogen, N_2. However, N_2 is taken to be chemically inert in the current analysis. This results in a stoichiometric oxygen-to-fuel ratio by mass s of 4.0 for methane–air combustion, and a stoichiometric mixture is considered for the current analysis.

This simplification of chemical mechanism is adopted for computational efficiency, as this analysis primarily focuses on the fluid-dynamical aspects of FWI, i.e., the statistics of the fluid-dynamical quantities, which are affected by the dilatation rate arising from exothermic chemical reactions and not directly by the chemical mechanism. The 1D head-on quenching simulations at different wall

temperatures, ranging from 300 to 750 K, with a skeletal mechanism involving 16 species and 25 reactions[15] demonstrated that the dilatation rate variation during flame–wall interaction remains almost within 3%–5% of the dilatation rate obtained from the single-step chemical reaction treatment. It is worth noting that several previous studies utilized single-step chemistry for head-on quenching simulations of premixed turbulent flames under initially isotropic turbulence conditions,[11,16–18] head-on quenching in a turbulent channel flow,[19] and also in a V-flame configuration.[1,20] It has been found that the previously proposed closures for the flame surface density (FSD) and scalar dissipation rate (SDR) based on simple chemistry DNS data are valid for detailed chemistry DNS data in the case of FWI.[21,22] Additionally, wall heat flux and wall Peclet number obtained from simple chemistry DNS are found to be in good agreement with experimental findings.[23–25] The fluid-dynamical aspects of oblique-wall quenching of turbulent V-shaped premixed flames based on simple chemistry DNS data[1,20] are consistent with detailed chemistry results.[2] The detailed chemistry-based DNS analyses[2,21,22,26] revealed that low-temperature chemical reactions originating from H, HO_2, and H_2O_2 can give rise to heat release at the chemically inert wall despite flame quenching. These effects are strong for hydrogen flames and weak for hydrocarbon flames.[2,21,22,26] This implies that the near-wall heat release effects will not be very relevant in the current work as in this work the flames are representative of methane-air combustion. Note that a recent detailed chemistry DNS-based FWI analysis of H_2–air flames by Zhao *et al.*[26] revealed that the wall-normal temperature profile and wall heat flux are not significantly affected by the presence of heat release at the wall. Consequently, the wall-normal temperature and heat flux will not be significantly affected by the heat release at the wall for hydrocarbon–air flames. In light of this information, it can be expected that the flow statistics in wall-bounded flows analyzed in this work can be captured at least qualitatively with the help of single-step chemistry.

The Lewis number for all species is assumed to be unity for the present analysis, with the unburned gas temperature T_R set at 730 K (because unburned gas is often preheated in spark ignition engines and gas turbines). This yields a Zel'dovich parameter, $\beta = T_a \times (T_{ad} - T_R)/T_{ad}^2$ of 6.0 (where T_a, T_{ad}, and T_R represent the activation, adiabatic, and reactant temperatures, respectively), along with a heat release rate parameter, $\tau = (T_{ad} - T_R)/T_R$ of 2.3. The wall temperature is taken to be the same as the unburned gas temperature and the heat release rate parameter which is consistent with several previous DNS analyses of flame–wall interaction.[12,20,27,28] Standard values are adopted for the Prandtl number, $Pr = 0.7$ and the ratio of specific heats $\gamma = 1.4$.

Simulations are conducted in a setup where turbulent boundary layers develop over a chemically inert wall.[29,30] Initial flow conditions for reacting flow simulations are generated based on fully developed, non-reacting turbulent channel flow solutions corresponding to $Re_\tau = \rho_R u_{\tau,NR} h/\mu_u = 110$ and 180, where $u_{\tau,NR} = \sqrt{|\tau_{w,NR}|/\rho_R}$ represents the friction velocity of the corresponding non-reacting channel flow, $\tau_{w,NR}$ is the wall shear stress, ρ_R is the unburned gas density, and h is the channel half-height. The sensitivity of the results on the value of Re_τ is considered in the paper by considering two different Reynolds numbers. The channel flow DNS with friction Reynolds number $Re_\tau = 180$ shows the self-similar behavior for mean velocity and turbulence statistics within the turbulent boundary layer.[31] It was demonstrated by Ghai *et al.*[32] that the wall-normal variations of dissipation rate of turbulent kinetic energy, vortex stretching, and dissipation terms of the enstrophy transport equation normalized by the wall units for fully developed channel flow with $Re_\tau = 110$ are found to be in good qualitative and quantitative agreement with experimental results of open boundary layer for $Re_\tau = 890$.[33] It was also demonstrated by Kai *et al.*[34] that the reactive scalar gradient statistics obtained from single-step chemistry DNS for $Re_\tau = 110$ are found to be qualitatively similar to those obtained for multi-step chemistry for $Re_\tau = 395$. The friction Reynolds number Re_τ considered in this analysis is comparable to the value used in several recent experimental investigations.[35–37]

The computational domain is taken to be a rectangular parallelopiped of dimensions $L_x \times L_y \times L_z = 10.69h \times 1.33h \times 4h$, which is discretized by equidistant Cartesian grids of dimension $1920 \times 240 \times 720$ and $3200 \times 400 \times 1200$ for $Re_\tau = 110$ and 180, respectively. Additionally, this grid ensures a maximum value of y^+ (dimensionless distance from the wall) not exceeding 0.6 for the grid points adjacent to the wall[38] and at least 8 grid points are accommodated within the thermal flame thickness $\delta_{th} = (T_{ad} - T_R)/\max|\nabla T|_L$, where T denotes the instantaneous dimensional temperature.

The bulk Reynolds numbers for the fully developed channel flow simulations used for initializing the flow field are $Re_b = 2\rho_R u_b h/\mu_R = 3285$ and 5665 for $Re_\tau = 110$ and 180, respectively. Here, $u_b = 1/2h \int_0^{2h} u dy$ represents the bulk mean velocity. The ratio of unstretched laminar burning velocity to the non-reacting flow friction velocity, denoted as $S_L/u_{\tau,NR}$, is assumed to be 0.7. The Mach number based on $u_{\tau,NR}$, expressed as $Ma = u_{\tau,NR}/a_0$ (where a_0 denotes the acoustic speed in the unburned gas), is 3×10^{-3} for all investigated cases. This Mach number is representative of stoichiometric methane–air mixture preheated to 730K under atmospheric condition and the local Mach number based on the centerline velocity of the fully developed channel flow for the Re_τ values considered here is approximately 20 times of $Ma = u_{\tau,NR}/a_0$. The Courant number based on a_0 is taken to be $Co = a_0 \Delta t/\Delta x = 0.1$ for the simulations conducted here. This time step size provides sufficient temporal resolution as well as numerical stability for the simulations.

The validation of non-reacting flow simulation results has been conducted by comparing them to previous research findings, particularly those reported by Tsukahara *et al.*[31] The achieved agreement, as documented in previous studies by Ahmed *et al.*,[20,39,40] confirms the reliability and accuracy of the simulations in capturing fundamental flow characteristics. The validation shown by Ahmed *et al.*[20,39,40] are not repeated here for the sake of brevity.

For these simulations, crucial parameters such as the longitudinal integral length scale L_{11} and the root mean square velocity fluctuation u' scale with the parameters h and $u_{\tau,NR}$, respectively, as delineated in the work by Ahmed *et al.*[41] These relationships yield values of Damköhler number $Da = L_{11} S_L/u' \delta_{th}$ of 15.80 and 26, and Karlovitz number $Ka = (u'/S_L)^{3/2} (L_{11}/\delta_{th})^{-1/2}$ of 0.36 and 0.28 for Re_τ of 110 and 180, respectively. These values indicate the regime of corrugated flamelets combustion when the flame remains away from the wall.[42]

The schematic diagram illustrating the HOQ configuration is presented in Fig. 1. Periodic boundary conditions are prescribed for the streamwise ($x-$) and spanwise ($z-$) directions, while the mean pressure gradient, expressed as $-\partial \overline{p}/\partial x = \overline{\rho} u_{\tau,NR}^2/h$ (where p denotes pressure), is applied in the streamwise flow direction. A no-slip

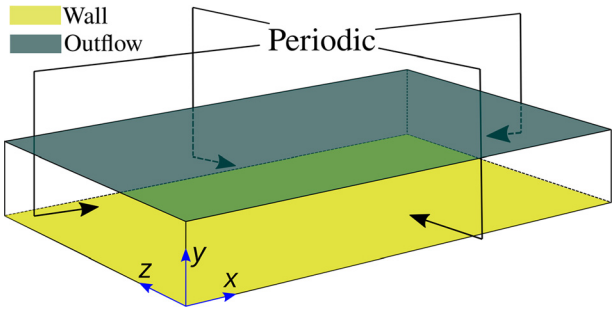

FIG. 1. Schematic diagram representing the simulation domain employed for the unsteady HOQ configuration.

boundary condition is implemented at $y = 0$, and the wall temperature T_w is set equal to the unburned gas temperature T_R, specified as $T_w = T_R = 730K$, indicating an isothermal wall boundary condition. The walls are considered to be impenetrable, which means wall-normal gradients of all the species at the wall are considered for the current analysis. At $y/h = 1.33$, a partially nonreflecting outflow boundary is prescribed based on the Navier–Stokes characteristic boundary conditions (NSCBC) proposed by Yoo and Im.[43] Initialization of the reacting flow field ensures that the reaction progress variable c attains a value of 0.5 at $y/h \approx 0.85$ with the unburned gas facing the wall. Here, the reaction progress variable c is defined in terms of the fuel mass fraction Y_F as $c = (Y_{FR} - Y_F)/(Y_{FR} - Y_{FP})$, where subscripts R and P represent the fresh reactant and fully burned products, respectively. This formulation ensures that c ranges from 0.0 in the unburned gas to 1.0 in the fully burned gas.

The simulation duration spans a maximum of 2.0 flow-through times, corresponding to 21.30 t_f and 30.3 t_f for Re_τ values of 110 and 180, respectively, where t_f represents the chemical timescale, defined as $t_f = \delta_{th}/S_L$. During the simulation period, the flame propagates toward the wall and interacts with it, while the boundary layer does not evolve significantly, consistent with the corresponding non-reacting flow simulation.[29,39,40] The Reynolds- and Favre-averaged quantities (where $\langle Q \rangle$ and $\widetilde{Q} = \langle \rho Q \rangle / \langle \rho \rangle$ are the Reynolds-averaged and Favre-averaged values of a variable Q, respectively), involving correlations of Reynolds and Favre fluctuations in the HOQ configuration under consideration, are determined by spatially averaging the relevant quantities in the periodic statistically homogeneous directions (i.e., $x - z$ planes) at a given time instant. The numerical differentiation used for DNS simulations is also adopted for the evaluation of spatial derivatives for the postprocessing operations.

III. MATHEMATICAL BACKGROUND

For the multiscale analysis conducted in this study, the DNS data have been filtered using an explicit filtering technique by employing the convolution of two or three 1D Gaussian filter kernel $G(r)$.[4] This filter modifies the values of a quantity Q by convolving it with the filter kernel $G(r)$ according to the following equation:[4,44]

$$\overline{Q(x)} = \int Q(x-r)G(r)dr \quad \text{and} \quad G(r) = \left(6/\pi\Delta^2\right)^{1/2} \exp\left(-6r \cdot r/\Delta^2\right), \tag{2}$$

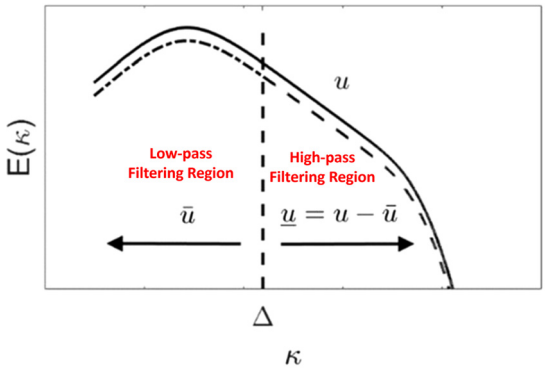

FIG. 2. Turbulent kinetic energy spectrum of velocity u_i (solid line) before using any filter. The dash-dotted line depicts the spectrum after applying a low-pass filter, resulting in $\bar{u}_i$ and the dashed line shows the spectrum after applying a high-pass filter, resulting in $\underline{u}_i = u_i - \bar{u}_i$. Both, high- and low-pass filtered spectra, are to be understood as sketches as the present work does not use a sharp spectral cutoff filter.

where Δ is the filter width. The application of this low-pass filter effectively removes high-wavenumber content from the fluctuating velocity signal, as depicted in Fig. 2. Additionally, a corresponding high-pass filter, which removes low-wavenumber content, is defined as $\underline{Q} = Q - \overline{Q}$. In the analysis conducted in this work, a number of filter widths have been employed ranging from $\Delta/h = 0.02$, where the flame is partially resolved, to $\Delta/h = 0.25$, where the flame becomes fully unresolved (i.e., Δ is of the order of the integral length scale).

It should be recognized here that in the non-periodic direction, filtering near the domain boundaries, such as walls, requires special attention.[9] Two options have been considered in this work, which are described below:

(i) Two-dimensional filter: In this approach, filtering is performed only in the periodic $x - z$ planes. The filter operation avoids extending into the direction perpendicular to these planes, which is the wall-normal direction. This approach simplifies the filtering process near boundaries but may not fully capture the anisotropies induced by the wall.

(ii) Three-dimensional asymmetric filter: In this approach, a three-dimensional filter kernel is used, but a special treatment is applied in the wall-normal direction close to the wall (i.e., $y-$ direction). When the wall-normal distance of a grid point is smaller than the filter width, the filter size in the $y-$ direction is taken to be the same as the wall-normal distance. After this operation, the filter kernel is renormalized to maintain the normalization condition $\int G(r)dr = 1.0$. This approach accounts for the wall boundary effects more accurately. A similar treatment is used for the other non-periodic boundaries of the domain. As the filters are normalized there is no *a priori* reason to conclude the relative strengths of 3D and 2D filtering techniques. However, the effect of filtering depends also on the flow structure, which changes most rapidly in wall-normal $y-$ direction. One could imagine a 2D filter of the form $G(x)G(y)$ would be stronger than $G(x)G(y)G(z)$ for the channel flow. Contrary, if the flow would be independent of the wall-normal direction, 2D and 3D filters would have exactly the same effect.

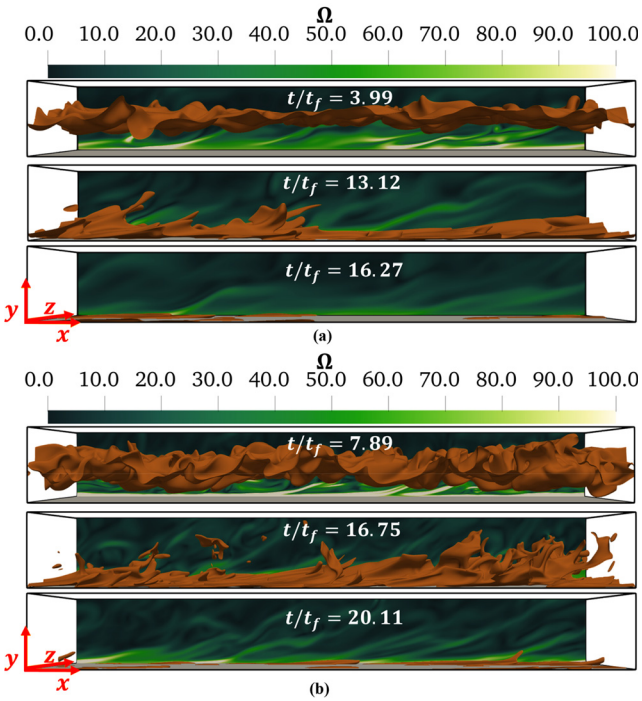

FIG. 3. Isosurfaces representing the reaction progress variable $c = 0.8$ are shown across various stages of HOQ of the turbulent premixed flame expressed in terms of t/t_f, (where $t_f = \delta_{th}/S_L$ denotes the chemical timescale) at (a) $Re_\tau = 110$ and (b) $Re_\tau = 180$. Additionally, the spatial distributions of normalized vorticity magnitude $\Omega = \sqrt{w_i w_i} \times h/u_{\tau,NR}$ are presented on the $x - y$ plane at $z/h = 4$.

It is to be noted that a Gaussian filter is not a sharp filter, but it is a homogeneous filter, which means that the filtering and differentiation operations commute for this filter, which is a convenient aspect. This aspect is not maintained for sharp filters, and they often introduce artificial aspects (e.g., sharp spectral filter introduces artificial overshoots and undershoots).[4] The top hat filter used in practical applications in physical space shows undulations in spectral space and is not sharp either. The methodology adopted in this paper is consistent with several previous analyses,[5,8,9] which analyzed the multiscale behavior of anisotropy in both reacting and non-reacting turbulent boundary layers.

The Gaussian filter is a low-pass filter, which mostly removes the information coming from the length scale smaller than the filter size Δ because the physics occurring at the length scale smaller than Δ becomes unresolved. Thus, the explicit filtering operation retains the low-pass filtered information, which is coming from the length scale greater than the filter size Δ. Therefore, subtracting the low-pass filtered data from the unfiltered variable (which includes both low- and high-pass information) yields the high-pass filtered information, which represents the information arising from the sub-filter scale. This is schematically illustrated in Fig. 2.

A multiscale analysis aimed at comprehensively examining and understanding the inherent anisotropy in Reynolds stress and dissipation rate tensors is performed. The anisotropy of Reynolds stress and viscous dissipation tensors can be expressed through the following tensors:[45,46]

$$b_{ij} = \widetilde{u''_{si}u''_{sj}}/2\widetilde{k}_s - \delta_{ij}/3 \quad \text{and} \quad d_{ij} = \widetilde{\varepsilon}^s_{ij}/2\widetilde{\varepsilon}^s - \delta_{ij}/3. \qquad (3)$$

Here, $\widetilde{k}_s = \widetilde{u''_{si}u''_{si}}/2$ denotes the turbulent kinetic energy, and $\widetilde{\varepsilon}^s = \langle \mu(\partial u''_{si}/\partial x_k)(\partial u''_{si}/\partial x_k)\rangle/\langle\rho\rangle = \widetilde{\varepsilon}^s_{ii}/2$ stands for its dissipation

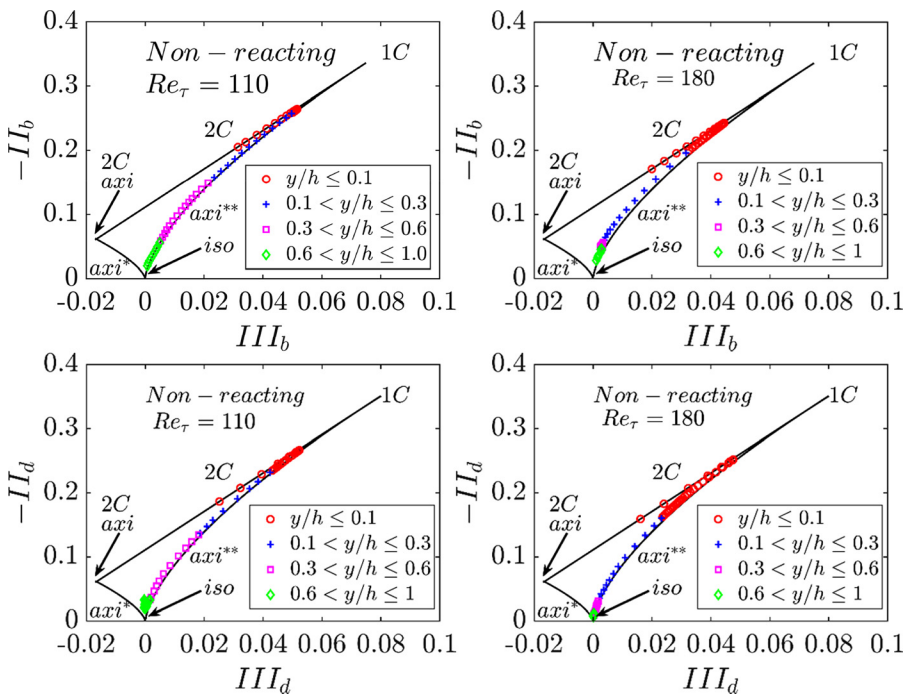

FIG. 4. Plots illustrating $-II_b$ vs III_b (1st row) for the Reynolds stress tensor and $-II_d$ vs III_d (2nd row) for the dissipation rate tensor are represented on the Lumley triangle for Re_τ values of 110 (1st column) and 180 (2nd column) for the non-reacting case. Note *axi** represents an axisymmetric contraction and *axi*** represents an axisymmetric expansion.

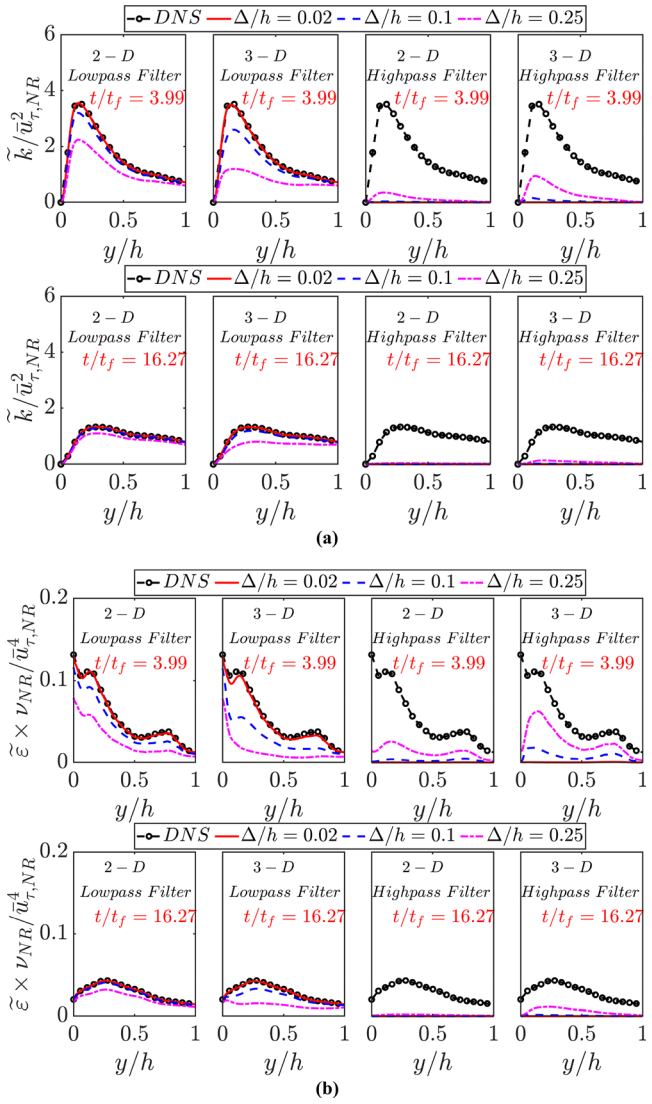

FIG. 5. Distributions of (a) $\widetilde{k}/u^2_{\tau NR}$ and (b) $\widetilde{\varepsilon} \times \nu_{NR}/\bar{u}^4_{\tau,NR}$ with y/h for unfiltered DNS data, as well as for 3D and 2D low-pass and high-pass filters with varying filter widths at $t/t_f = 3.99$ and 16.27 for $Re_\tau = 110$.

rate. Here, u_{si} is the ith component of either unfiltered velocity or low-pass filtered velocity or high-pass filtered velocity, as appropriate, the double prime denotes the Favre averaged fluctuation.

While the first invariants of these tensors vanish due to their trace-free nature (i.e., $b_{ii} = d_{ii} = 0$), the second (i.e., II_b and II_d), and third invariants (i.e., III_b and III_d) are expressed as follows:[45,46]

$$II_b = -b_{ij}b_{ji}/2 \quad \text{and} \quad II_d = -d_{ij}d_{ji}/2, \tag{4}$$

$$III_b = b_{ij}b_{jk}b_{ki}/3 \quad \text{and} \quad III_d = d_{ij}d_{jk}\mathrm{d}_{ki}/3. \tag{5}$$

These invariants, as outlined in Eqs. (4) and (5), influence the eigenvalues of the anisotropy tensors, subsequently affecting the characteristic equations of b_{ij} and d_{ij}. The eigenvalues, in turn, categorize the realizable states of turbulence into distinct boundaries[45,46]

- In the 1-component (1C) corner, only one eigenvalue of $\widetilde{u''_{si}u''_{sj}}$ or $\widetilde{\varepsilon}_{ij}$ is non-zero, resulting in eigenvalues of the anisotropy b_{ij} and d_{ij} tensor as $\{\lambda_1, \lambda_2, \lambda_3\} = \{2/3, -1/3, -1/3\}$.
- The 2-component (2C) axisymmetric corner features two non-zero eigenvalues of $\widetilde{u''_{si}u''_{sj}}$ or $\widetilde{\varepsilon_{ij}}$, yielding eigenvalues of the anisotropy b_{ij} and d_{ij} tensor as $\{\lambda_1, \lambda_2, \lambda_3\} = \{1/6, 1/6, -1/3\}$.
- In the 3-component (3C) isotropy corner, all three eigenvalues of $\widetilde{u''_{si}u''_{sj}}$ or $\widetilde{\varepsilon}_{ij}$ are non-zero and equal, resulting in eigenvalues of the anisotropy b_{ij} and d_{ij} tensor as $\{\lambda_1, \lambda_2, \lambda_3\} = \{0, 0, 0\}$.

The borders connecting the limiting eigenvalues of the anisotropy tensors play a crucial role in delineating the different states of turbulence, as described in the literature.[46] In the 2-component limit, two eigenvalues are unequal and non-zero, while the third eigenvalue is zero (such as $\lambda_1 > \lambda_2$ and $\lambda_3 = 0$). For the axisymmetric expansion, one eigenvalue dominates over the other two (such as $\lambda_1 > \lambda_2 = \lambda_3$), reflecting rod-like turbulence structures where flow elongation is prominent. Conversely, in axisymmetric compression, two eigenvalues are significantly larger than the third (such as $\lambda_1 = \lambda_2 > \lambda_3$), characterizing disc-like turbulence structures. It is worth noting that all feasible turbulence states fall within the so-called Lumley triangle, bound by these borders and vertices.[46]

IV. RESULTS AND DISCUSSION

A. Instantaneous scalar field

The instantaneous views of the reaction progress variable $c = 0.8$ isosurfaces at non-dimensional times such as $t/t_f = 3.99\,(7.89)$, $13.12\,(16.75)$ and $16.25\,(20.11)$ for $Re_\tau = 110$ (180) are shown in Fig. 3 along with the spatial distributions of normalized vorticity magnitude $\Omega = \sqrt{w_i w_i} \times h/u_{\tau,NR}$ on the $x - y$ plane at $z/h = 4$. The choice of $c = 0.8$ is motivated by the fact that the peak value of reaction rate of the reaction progress variable occurs at $c \approx 0.8$ for the unstretched, steady laminar premixed flame so this isosurface can be considered as the flame surface. The time instants $t/t_f = 3.99$ $(t/t_f = 7.89)$, $t/t_f = 13.12$ $(t/t_f = 16.75)$, and $t/t_f = 16.27\,(t/t_f = 20.11)$ for the $Re_\tau = 110$ $(Re_\tau = 180)$ case correspond to the normalized wall-normal distance of $y/h = 0.72$, 0.06, and 0.03 of the non-dimensional Favre-mean temperature $\widetilde{\theta} = (\widetilde{T} - T_0)/(T_{ad} - T_0) = 0.5$ isosurface, respectively. Thus, Fig. 3 provides an insight into the temporal evolution of flame dynamics within turbulent boundary layers during HOQ. The wrinkling of the flame surface shown in Fig. 3 is a result of the intricate interplay between turbulent shear and vortical motion. However, close to the wall, these wrinkles are attenuated, a phenomenon attributed to flame quenching due to wall heat loss and decay of turbulence in the vicinity of the wall. The wall shear stress τ_w for both Re_τ values decreases by 50% toward the end of flame quenching, which suggests that Re_τ decreases roughly by 30% at the end of quenching. The normalized minimum quenching distance is $y_Q/\delta_Z = 1.71\,(1.72)$ for the $Re_\tau = 110$ (180) case where $\delta_Z = \alpha_{T0}/S_L$ represents the Zeldovich flame thickness, α_{T0} denotes the thermal diffusivity in the unburned gas, and y_Q signifies the minimum wall-normal distance of the $\theta \approx 0.8$ isosurface. The consequence of the flame quenching is evident in the fragmented appearance of the flame surface at later times. The presence of the flame within the turbulent boundary layer induces predominantly positive dilatation rates $(\partial u_i/\partial x_i > 0)$, which influence turbulence statistics through flame-normal acceleration resulting from thermal expansion.

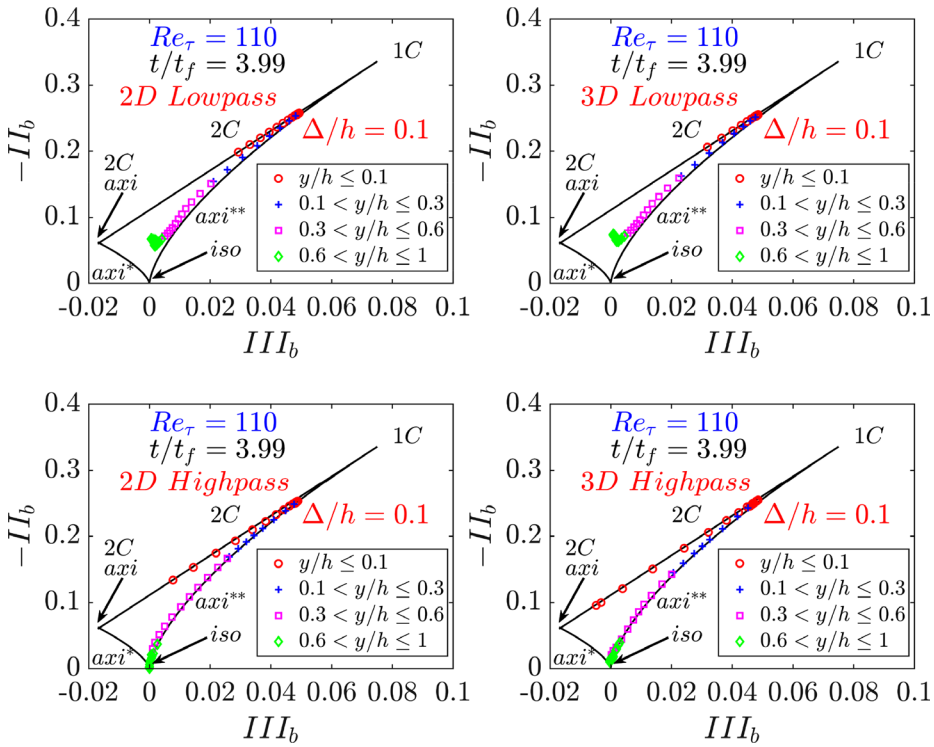

FIG. 6. Plots illustrating $-II_b$ vs III_b for the Reynolds stress tensor are represented on the Lumley triangle for Re_τ values of 110 for (2D and 3D) low-pass and high-pass filter width of $\Delta/h = 0.1$ at $t/t_f = 3.99$. Note *axi** represents an axisymmetric contraction and *axi*** represents an axisymmetric expansion.

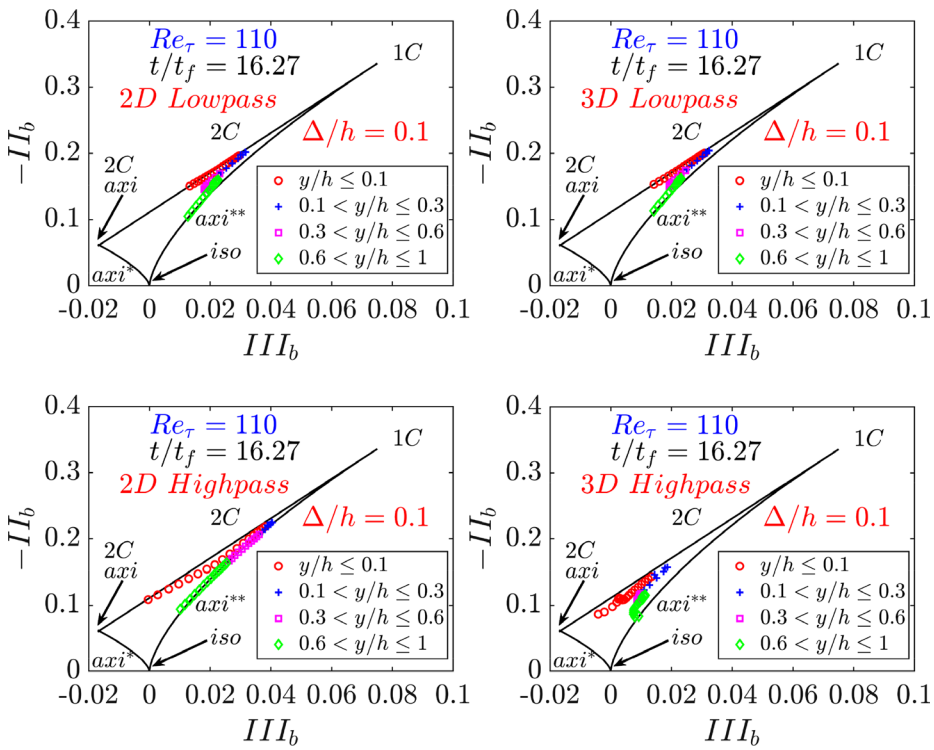

FIG. 7. Plots illustrating $-II_b$ vs III_b for the Reynolds stress tensor are represented on the Lumley triangle for Re_τ values of 110 for (2D and 3D) low-pass and high-pass filter width of $\Delta/h = 0.1$ at $t/t_f = 16.27$. Note *axi** represents an axisymmetric contraction and *axi*** represents an axisymmetric expansion.

B. Anisotropy in non-reacting channel flow

In order to understand the multiscale nature of the Reynolds stress and dissipation tensors across a wide range of scales, denoted by different filter sizes, for HOQ of premixed flames propagating across turbulent boundary layers, the anisotropies of the Reynolds stress and dissipation tensor from a non-reacting channel flow simulation, exemplified in the form of the Lumley triangle, are shown in terms of the plots of $-II_b$ vs III_b and $-II_d$ vs III_d in Fig. 4 for Re_τ values of 110 and 180. Figure 4 illustrates that the second and third invariants of the anisotropy tensors for the Reynolds stress and dissipation tensors exhibit almost identical qualitative trends, with slightly more tendency toward isotropy observed for the dissipation tensor as the center of the channel is approached. This observation remains consistent with the earlier findings from turbulent channel flow[9] and aligns with early experimental data from turbulent boundary layers by Antonia *et al.*[46]

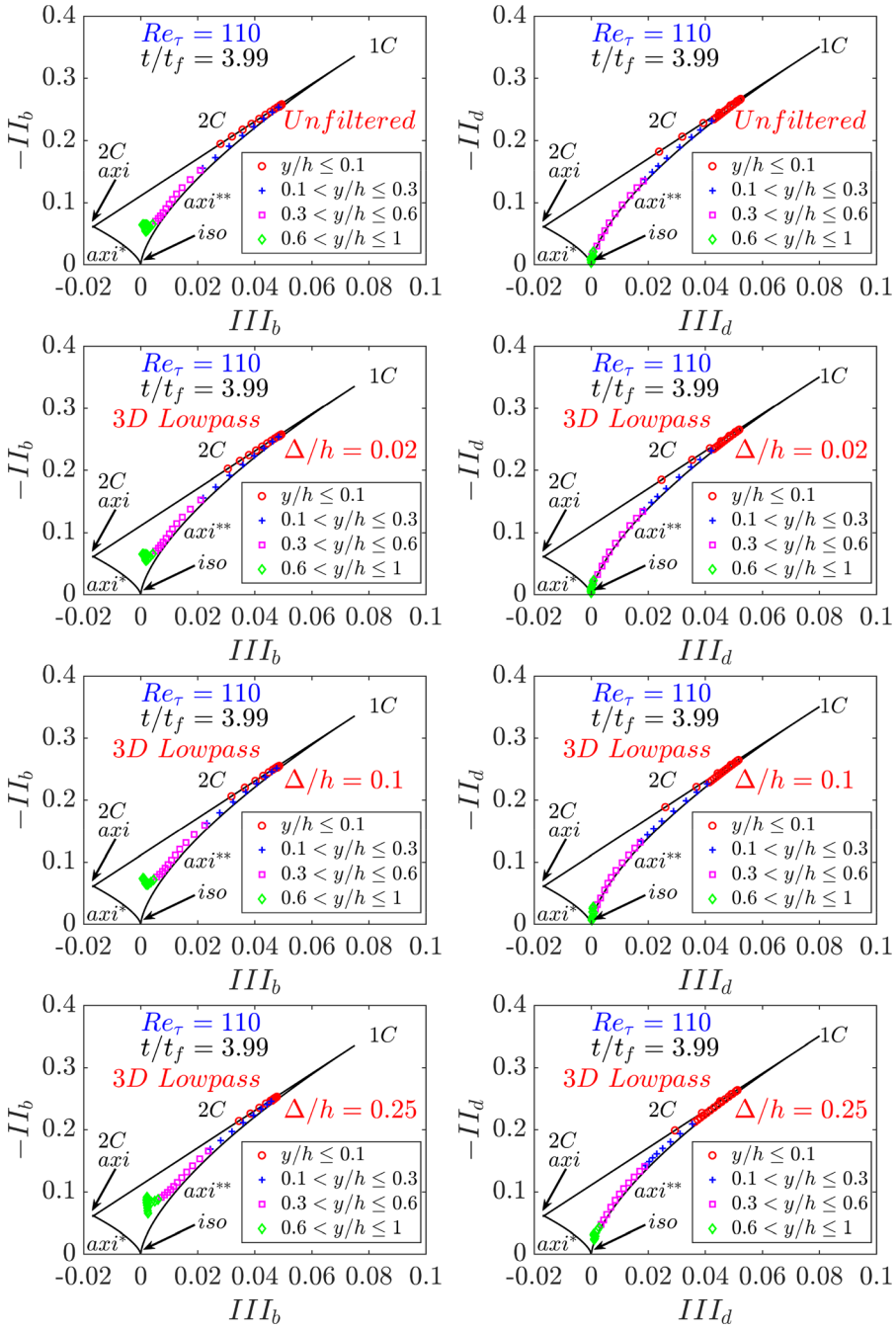

FIG. 8. Plots illustrating $-II_b$ vs III_b for the Reynolds stress tensor (left column) and $-II_d$ vs III_d (right column) for the dissipation rate tensor are represented on the Lumley triangle for unfiltered DNS data and 3D low-pass filter with varying filter widths at $t/t_f = 3.99$ for $Re_\tau = 110$.

In the viscous sublayer of the channel flow, turbulence is predominantly 2-component, with fluctuations of v being significantly smaller than fluctuations of u and w where u, v, and w are the velocity components in x, y, and z, respectively. Subsequently, there is a tendency toward the 1-component limit for small values of y/h caused by the increasing dominance of the axial velocity fluctuations. This is followed by an axisymmetric expansion where $u' > v' \approx w'$ before ultimately approaching isotropy near $y/h = 1.0$.[4] The tendency of isotropy is stronger toward the center of the channel with an increase in the value of the turbulent Reynolds number, Re_τ, while anisotropy tends to increase at the wall with an increase in Re_τ.

C. Comparison between 2D and 3D filtering

The variation of normalized turbulent kinetic energy $\widetilde{k}/u^2_{\tau NR}$ and its dissipation rate $\widetilde{\varepsilon} \times \nu_{NR}/\overline{u}^4_{\tau,NR}$ are shown in Fig. 5 for unfiltered

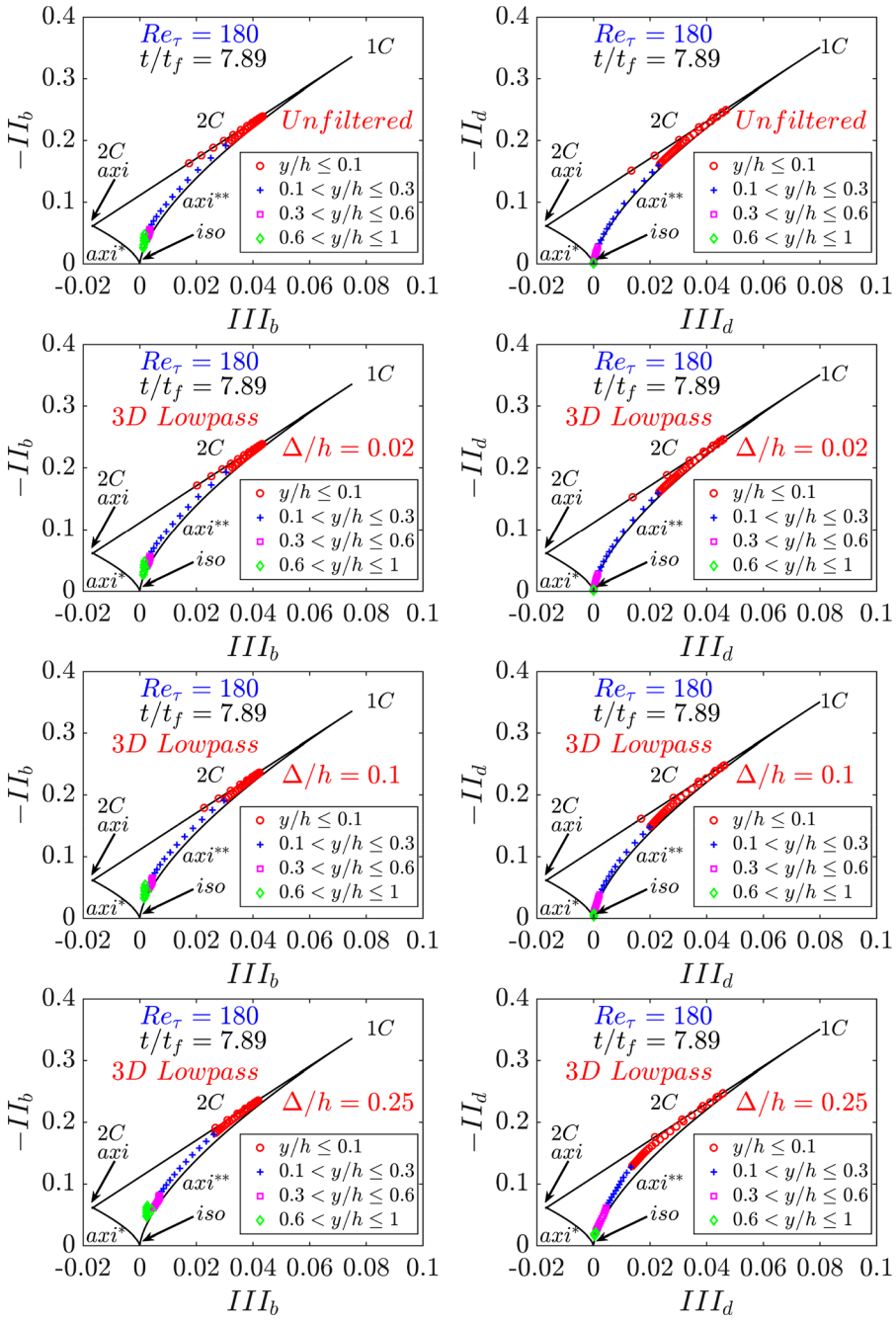

FIG. 9. Plots illustrating $-II_b$ vs III_b for the Reynolds stress tensor (left column) and $-II_d$ vs III_d (right column) for the dissipation rate tensor are represented on the Lumley triangle for unfiltered DNS data and 3D low-pass filter with varying filter widths at $t/t_f = 7.89$ for $Re_\tau = 180$.

DNS data along with the corresponding data for the 2D and 3D low-pass and high-pass filters with varying filter widths at $t/t_f = 3.99$ and 16.27 for $Re_\tau = 110$. The time instants at $t/t_f = 7.89$ and 20.11 for $Re_\tau = 180$ show similar qualitative behavior as that of the $t/t_f = 3.99$ and 16.27 for $Re_\tau = 110$, respectively, and are therefore not shown here for the sake of brevity. As discussed previously in Sec. II, a series of filter widths has been employed such as $\Delta/h = 0.02$, 0.1, and 0.25. It is noteworthy that the smallest (low-pass) filter width considered here corresponds to the condition at which the flame is partially resolved, while the normalized filter widths $\Delta/h = 0.1$ and 0.25 correspond to $\Delta > \delta_{th}$ where the flame becomes fully unresolved. Notably, the application of low-pass filters results in a gradual decrease in turbulent kinetic energy magnitude as the filter width increases. Similarly, the dissipation rate of turbulent kinetic energy also follows a decreasing trend with increasing filter size as a result of the convolution operation associated with low-pass filtering. This phenomenon is

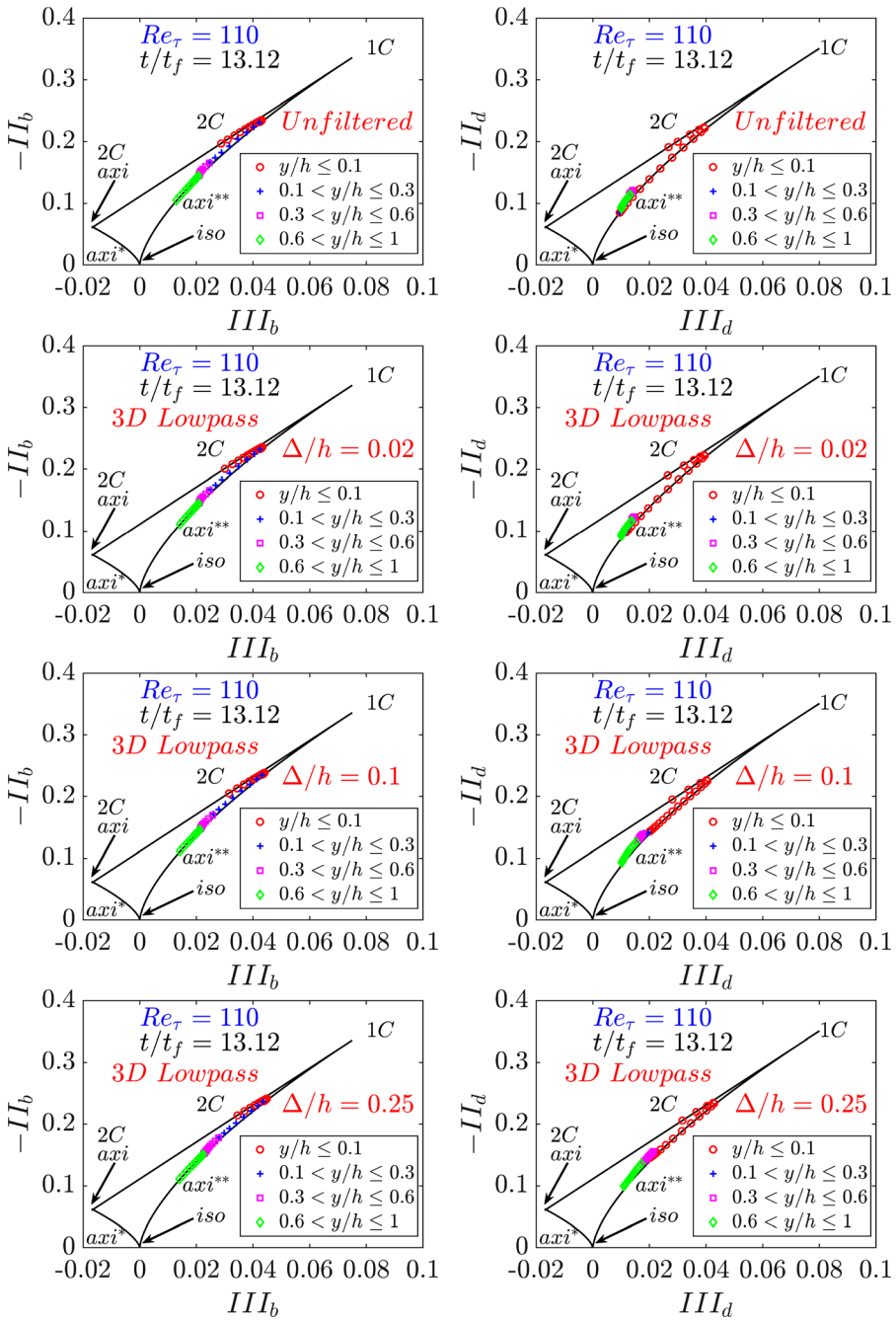

FIG. 10. Plots illustrating $-II_b$ vs III_b for the Reynolds stress tensor (left column) and $-II_d$ vs III_d (right column) for the dissipation rate tensor are represented on the Lumley triangle for unfiltered DNS data and 3D low-pass filter with varying filter widths at $t/t_f = 13.12$ for $Re_\tau = 110$.

consistent with the expected behavior, as low-pass filters effectively attenuate high-wavenumber turbulent fluctuations while preserving larger scale flow features. Consequently, the suppression of small-scale turbulent structures leads to a reduction in turbulent kinetic energy and its dissipation rate magnitude with an increase in the filter width. Conversely, the application of high-pass filters shows an opposite trend, with turbulent kinetic energy and its dissipation rate magnitude increasing as the filter width increases. High-pass filters preserve high-wavenumber turbulent fluctuations while suppressing lower wavenumber components, thereby emphasizing small-scale turbulent structures where energy dissipation occurs more rapidly. It is worth noting that dissipation rate peaks at the wall for the low-pass filter when the flame is away from the wall which is not the case for the high-pass filter. This shows interestingly that dissipation is contributed by to a considerable extent by large-scale structures, which is to some extent counterintuitive. There is a strong qualitative change in this

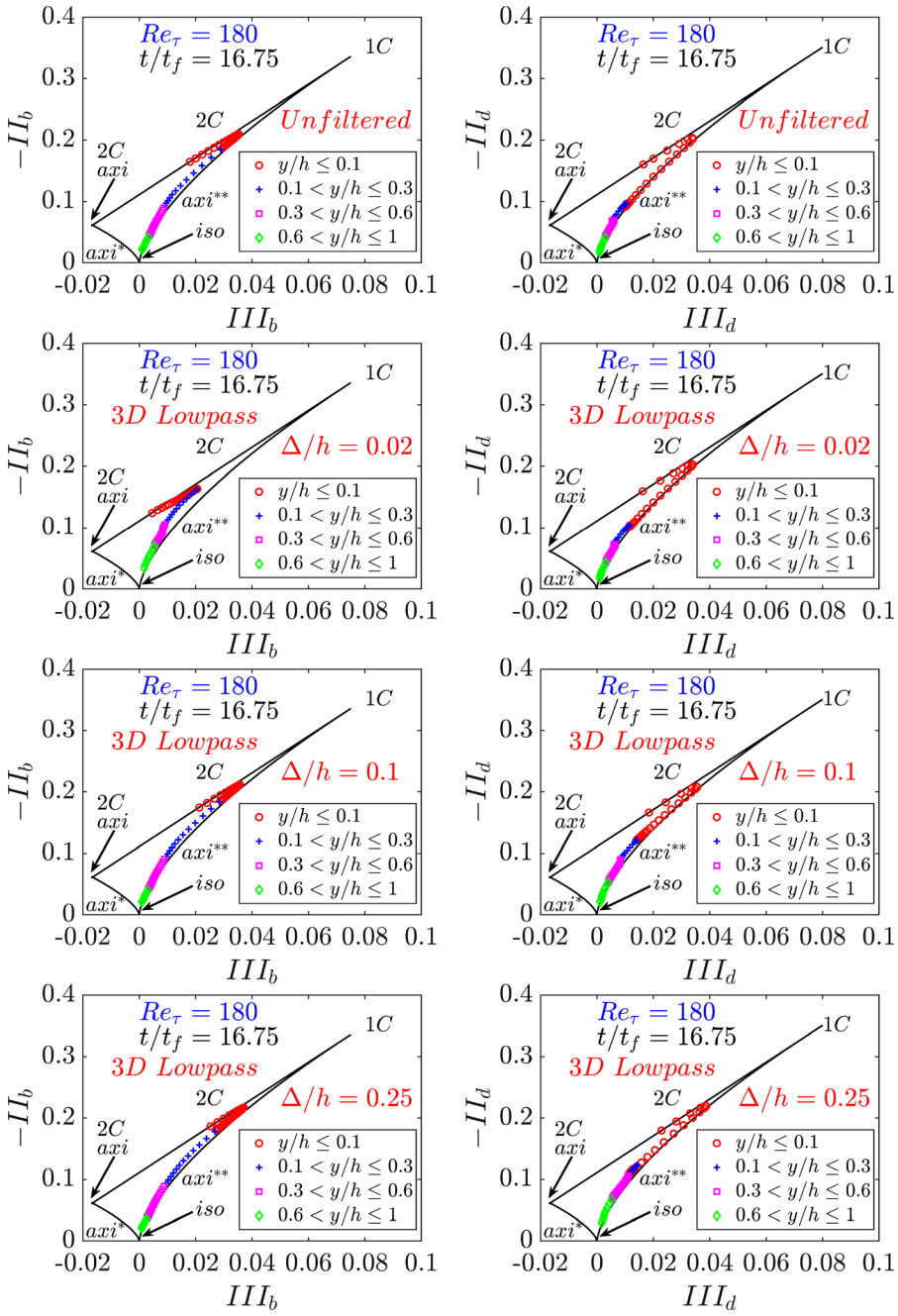

FIG. 11. Plots illustrating $-II_b$ vs III_b for the Reynolds stress tensor (left column) and $-II_d$ vs III_d (right column) for the dissipation rate tensor are represented on the Lumley triangle for unfiltered DNS data and 3D low-pass filter with varying filter widths at $t/t_f = 16.75$ for $Re_\tau = 180$.

picture after the flame has interacted with the boundary layer as can be seen at $t/t_f = 16.27$. At this point, the interaction of the flame with the boundary layer induces significant alterations in the flow dynamics, leading to a redistribution of Reynolds stresses and a shift in the dissipation patterns. This interaction highlights the complex interplay between turbulent structures and boundary conditions, which necessitates a deeper investigation to fully understand the underlying mechanisms driving these changes. In addition to the distinct trends in the magnitude of turbulent kinetic energy and its dissipation rate with varying filter widths, there exist significant differences between the 2D and 3D filtering options. The magnitude of turbulent kinetic energy and dissipation is higher (lower) with the 2D low-pass (high-pass) filter compared to the 3D low-pass (high-pass) filter for a given filter width. While the 2D filter captures the correct qualitative trend of turbulent kinetic energy and its dissipation, the 3D filter offers a more comprehensive representation of the multiscale nature of turbulent flow dynamics. These findings underscore the importance of considering filtering dimensionality accurately while analyzing turbulence

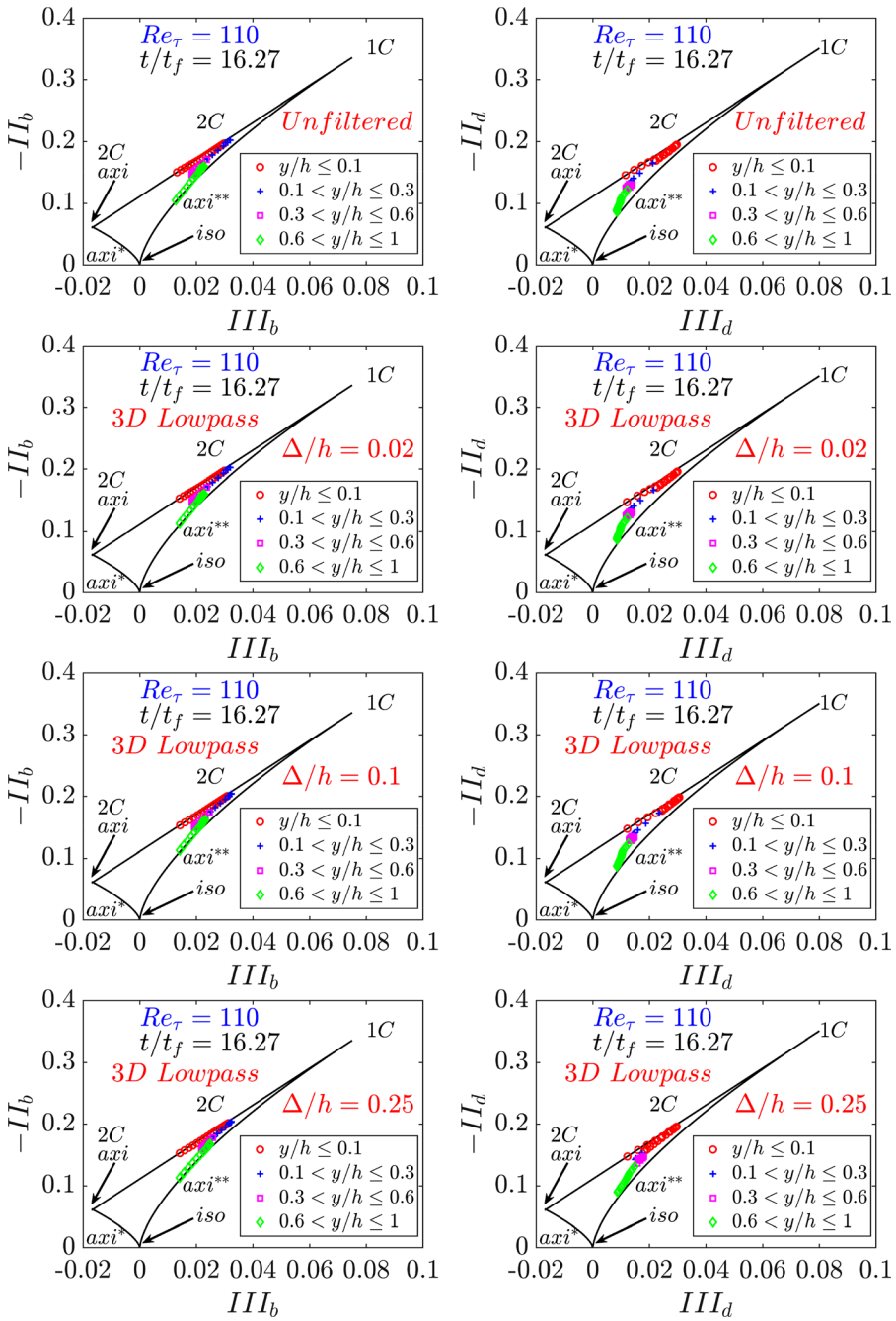

FIG. 12. Plots illustrating $-II_b$ vs III_b for the Reynolds stress tensor (left column) and $-II_d$ vs III_d (right column) for the dissipation rate tensor are represented on the Lumley triangle for unfiltered DNS data and 3D low-pass filter with varying filter widths at $t/t_f = 16.27$ for $Re_\tau = 110$.

phenomena, particularly, in scenarios such as HOQ of premixed flames in turbulent boundary layers, where interactions between turbulence and combustion are critical.

The results for the anisotropy of the Reynolds stress tensor are presented in Figs. 6 and 7 for both low-pass and high-pass filters. These results correspond to both 2D and 3D filtering with a ratio of $\Delta/h = 0.1$, obtained at a specific time instant when the flame is away from the wall, at $t/t_f = 3.99$ as well as when the flame interacts with the wall, at $t/t_f = 16.27$ for $Re_\tau = 110$. The 2-component limit is predominantly noticeable close to the wall, shifting toward the 1-component corner for values of $y/h \approx 0.1$. Following this transition, there is a gradual progression along the axisymmetric expansion boarder toward the isotropic limit as y/h approaches 1.0. However, with the progress of FWI, the convergence toward the isotropic limit diminishes for both 2D and 3D low-pass and high-pass filtering. Both 2D and 3D filtering demonstrate qualitatively similar trends across the two distinct filtering methodologies. In particular for regions in very close proximity to the wall, there is no discernible difference between

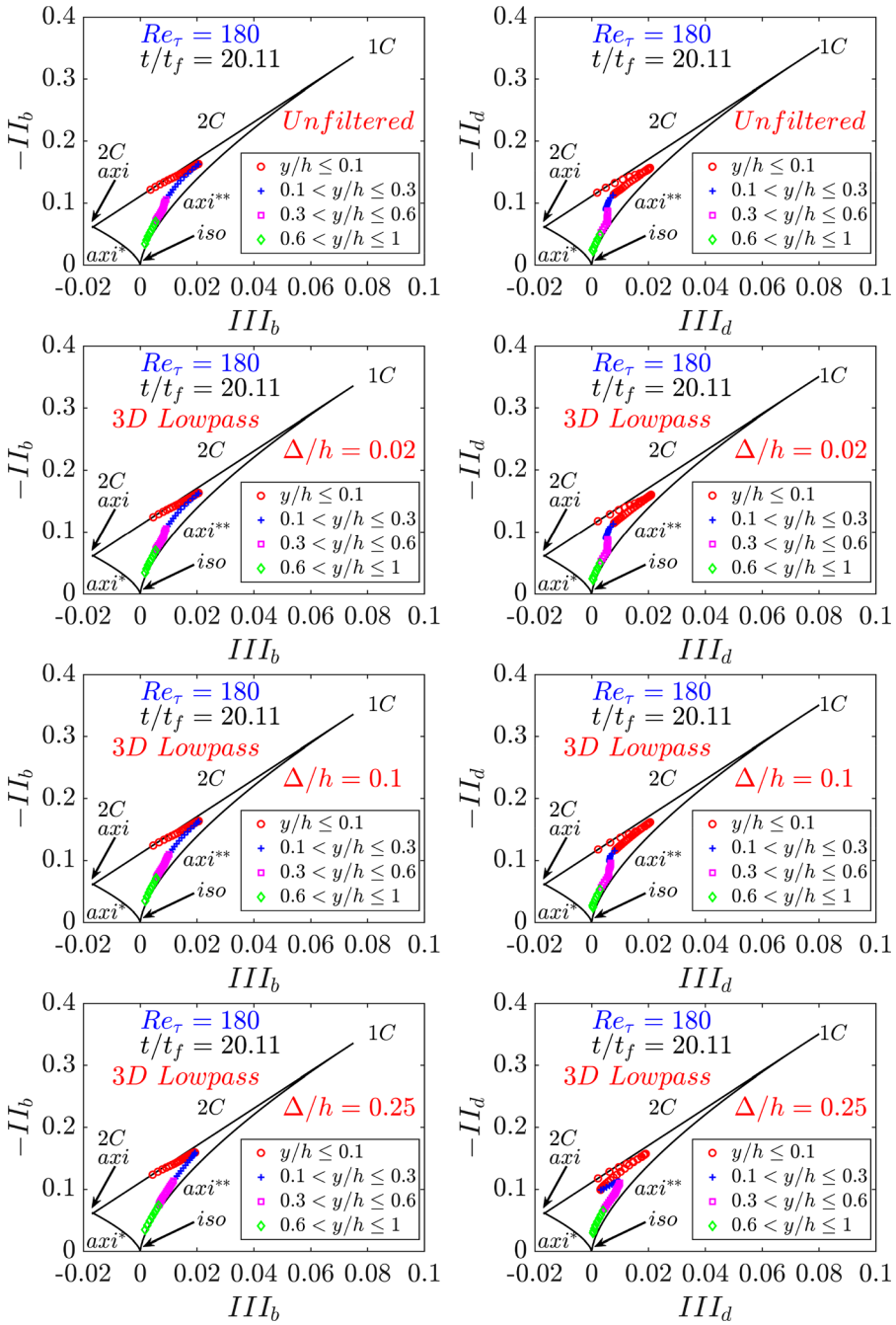

FIG. 13. Plots illustrating $-II_b$ vs III_b for the Reynolds stress tensor (left column) and $-II_d$ vs III_d (right column) for the dissipation rate tensor are represented on the Lumley triangle for unfiltered DNS data and 3D low-pass filter with varying filter widths at $t/t_f = 20.11$ for $Re_\tau = 180$.

the outcomes of the 2D and 3D low-pass filters. It is worth noting that the upward trend toward the 1C limit is slightly more pronounced in the results of the 3D low-pass filters compared to the 2D low-pass filters near the center of the channel (see upper part of Fig. 6). Nonetheless, in the case of high-pass filtering, a downward shift toward the isotropic limit is discernible in the 3D filter results near the channel center, which is more visible at $t/t_f = 16.27$ for $Re_\tau = 110$ but this trend can be discerned from the magenta colored points at $t/t_f = 3.99$. The downward shift toward the isotropic limit observed in the 3D filter results near the center of the channel in the case of high-pass filtering can be attributed to the ability of the 3D filtering to more effectively attenuate large-scale anisotropic turbulent structures. High-pass filtering primarily removes low-wavenumber components from the flow field, emphasizing the contribution of smaller scale turbulent motions. In turbulent boundary layer flows, there exists a dominance of large-scale streamwise-oriented structures due to the influence of the wall. These structures contribute significantly to the anisotropic nature of turbulence in the near-wall region. When applying the 3D filter, which filters in all spatial dimensions, it acts to suppress these large-scale anisotropic structures more effectively compared to the 2D filter. As a result, the high-pass filtered flow field exhibits a reduced influence of these anisotropic structures, leading to a shift toward the isotropic limit. This shift signifies a more isotropic distribution of turbulent energy across different spatial scales, indicating that the filtering process is successful in attenuating the dominance of large-scale anisotropic motions within turbulent boundary layers. Upon comparing Figs. 6 and 7 it becomes also clear that the range of values of $|III_b|$ and $|II_b|$ becomes increasingly narrow with the progress of FWI. While the dilatation influences the isotropy away from the wall, the interaction of the flame with the wall leads to a considerable alteration of the boundary layer turbulence which reduces the predominance of the axial velocity fluctuations. Henceforth, the results presented for the Lumley triangle are obtained through the application of a 3D filtering technique, encompassing both low-pass and high-pass filtering methodologies. This choice is based on its established efficacy in capturing three-dimensional flow features within turbulent boundary layers. Although Figs. 6 and 7 reveal that the results using 2D and 3D filters are qualitatively similar, 2D filtering is found to be approximately 20% faster to apply compared to 3D filtering for the considered datasets. This suggests that the multiscale analysis with a 2D filter will be sufficient to obtain the same qualitative results as that of the 3D results.

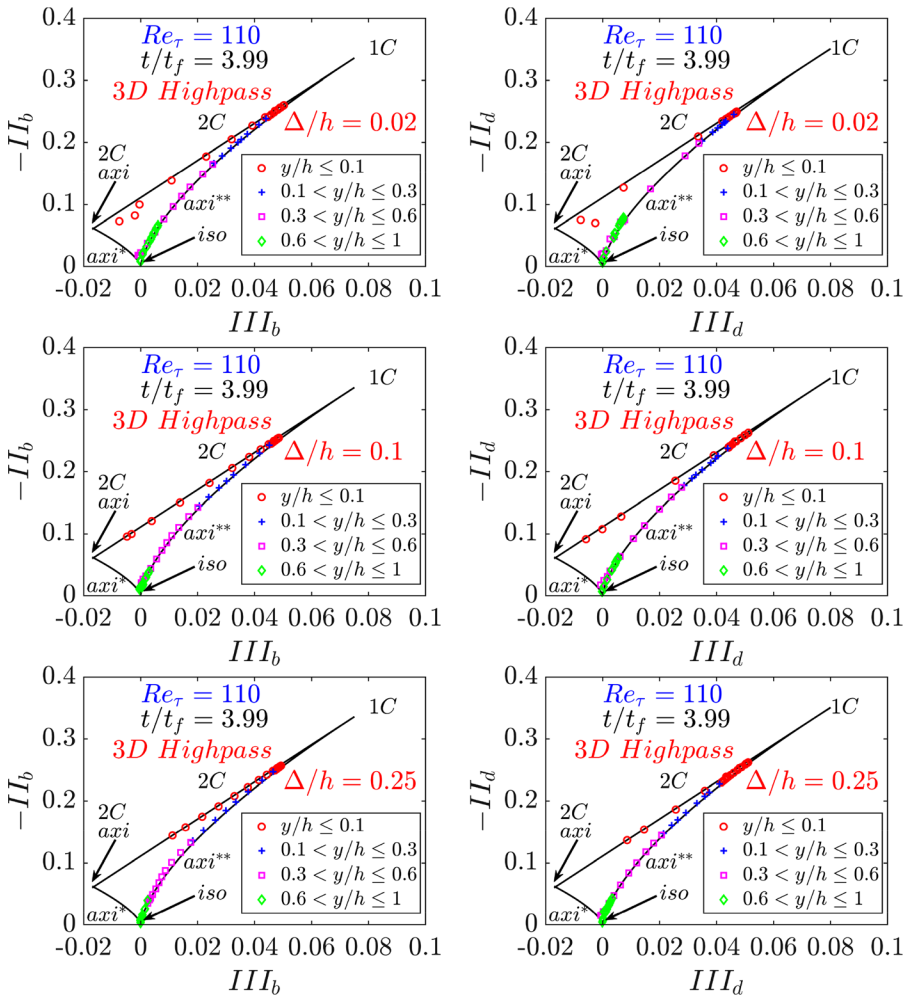

FIG. 14. Plots illustrating $-II_b$ vs III_b for the Reynolds stress tensor (left column) and $-II_d$ vs III_d (right column) for the dissipation rate tensor are represented on the Lumley triangle for 3D high-pass filter with varying filter widths at $t/t_f = 3.99$ for $Re_\tau = 110$.

D. Low-pass filter results

The comparative analysis between $-II_b$ and III_b for the Reynolds stress tensor, as well as $-II_d$ and III_d for the dissipation rate tensor, is presented in the form of the Lumley triangle in Figs. 8–13 for both unfiltered DNS data and the filtered data using a 3D low-pass filter with varying filter widths at different stages of HOQ (e.g., $t/t_f = 3.99$, 13.12, and 16.27, respectively) for $Re_\tau = 110$ and (e.g., $t/t_f = 7.89$, 16.75, and 20.11, respectively) $Re_\tau = 180$. Figure 10 reveals that at $t/t_f = 3.99$, the unfiltered data for the reacting flows case exhibits a behavior akin to the non-reacting channel flow results depicted in Fig. 4. Notably, the attainment of the 2-component limit is primarily observed near the wall, transitioning toward the 1-component corner for lower values of y/h. Subsequent to this transition occurring, a tendency toward the isotropic limit is observed as y/h approaches 1.0. It can be seen from Figs. 8, 10, and 12 for $Re_\tau = 110$ and Figs. 9, 11, and 13 for $Re_\tau = 180$ that the tendency toward the isotropy for the unfiltered data becomes weaker with the progress of HOQ. Furthermore, it is evident from Figs. 8–13 that an intriguing transition occurs from a 2-component elliptical limit to a 1-component limit very close to the wall as the filter width increases, in particular at early stages of FWI. This transition suggests a notable change in the dominant flow patterns or structures, potentially indicating a more constrained/organized flow regime in close proximity to the wall. This phenomenon is observed to diminish as the FWI progresses. Moreover, the observed decrease in isotropy as filter width increases underscores the anisotropic nature of the large-scale flow features. This reduction in isotropy hints at a growing influence of coherent flow patterns. The behaviors of the second and third invariants of Reynolds stress tensor remain qualitatively similar to the dissipation rate tensor at all stages of FWI. Particularly, this similarity in behavior between these tensors suggests a close relationship between the viscous dissipation rate and the Reynolds stress distribution within the flow. The noted stronger tendency toward isotropy in the dissipation rate tensor, consistent with the assumption that dissipation occurs at

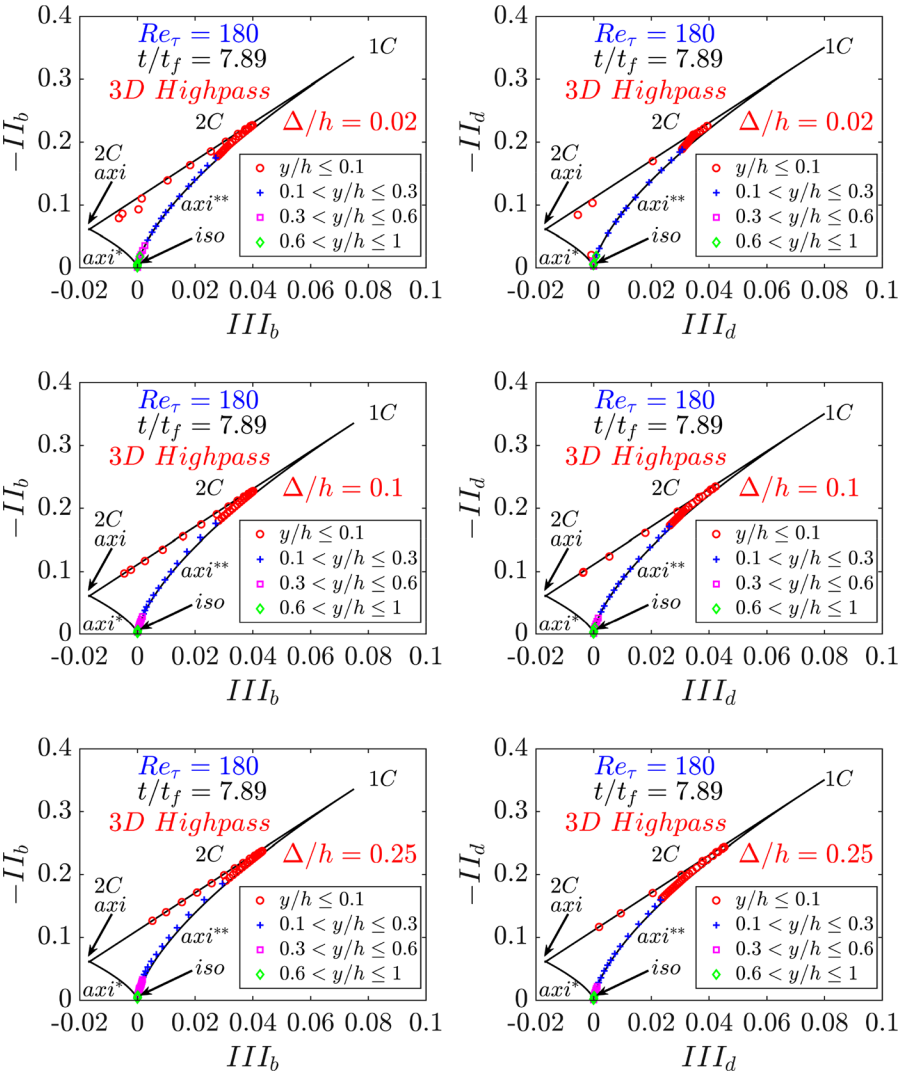

FIG. 15. Plots illustrating $-II_b$ vs III_b for the Reynolds stress tensor (left column) and $-II_d$ vs III_d (right column) for the dissipation rate tensor are represented on the Lumley triangle for 3D high-pass filter with varying filter widths at $t/t_f = 7.89$ for $Re_\tau = 180$.

smaller, more isotropic scales, when the flame is away from the wall (i.e., $t/t_f = 3.99$ and 7.89), indicates a more uniform dispersion of energy dissipation across various flow directions. This tendency becomes more pronounced for an increase in Reynolds number, signifying a heightened influence of flow dynamics on isotropic behavior. However, as the FWI progresses, an interesting reversal in this trend is observed. This reversal suggests a shift in the flow dynamics leading to a weakening of the isotropic tendency in the dissipation rate tensor as the FWI progresses. The anisotropy at later stages of FWI is probably induced by (in the mean) unidirectional flame-normal acceleration due to thermal expansion combined with an increase in kinematic viscosity on the burned gas side, which results in an increase in flow structures, together with a decrease in local Reynolds number. This evolution of anisotropy underscores the intricate nature of turbulence dynamics and its interaction with flame and wall boundaries.

E. High-pass filter results

The comparative analysis between $-II_b$ and III_b for the Reynolds stress tensor, as well as $-II_d$ and III_d for the dissipation rate tensor, is presented in the form of the Lumley triangle in Figs. 14–19 for the data filtered using a 3D high-pass filter with varying filter widths at different stages of HOQ of FWI (e.g., $t/t_f = 3.99$, 13.12, and 16.27, respectively) for $Re_\tau = 110$ and (e.g., $t/t_f = 7.89$, 16.75, and 20.11, respectively) $Re_\tau = 180$. It is recalled that, in contrast to the low-pass filter, the high-pass filter has the weak influence for large filter widths. As previously illustrated and discussed, the analysis of unfiltered data reveals a progressive increase in anisotropy with the advancement of FWI. Analogously, a comparable trend is evident in the findings derived from the utilization of a 3D high-pass filter: the anisotropy amplifies in tandem with the evolution of FWI, further accentuated by an increase in filter width for the 3D high-pass filter. It is noteworthy, that for late stages of FWI, the turbulence populates increasingly regions in the inner part of the Lumley triangle in contrast to non-reacting channel flow where it follows more or less closely the border of the Lumley triangle. Correspondingly, as the Reynolds number increases, a comparative decrease in anisotropy is observed, indicating a tendency toward the isotropic limit. Notably, the dissipation rate tensor demonstrates a greater degree of isotropy at a specified filter width and Reynolds number in comparison to the Reynolds stress tensor.

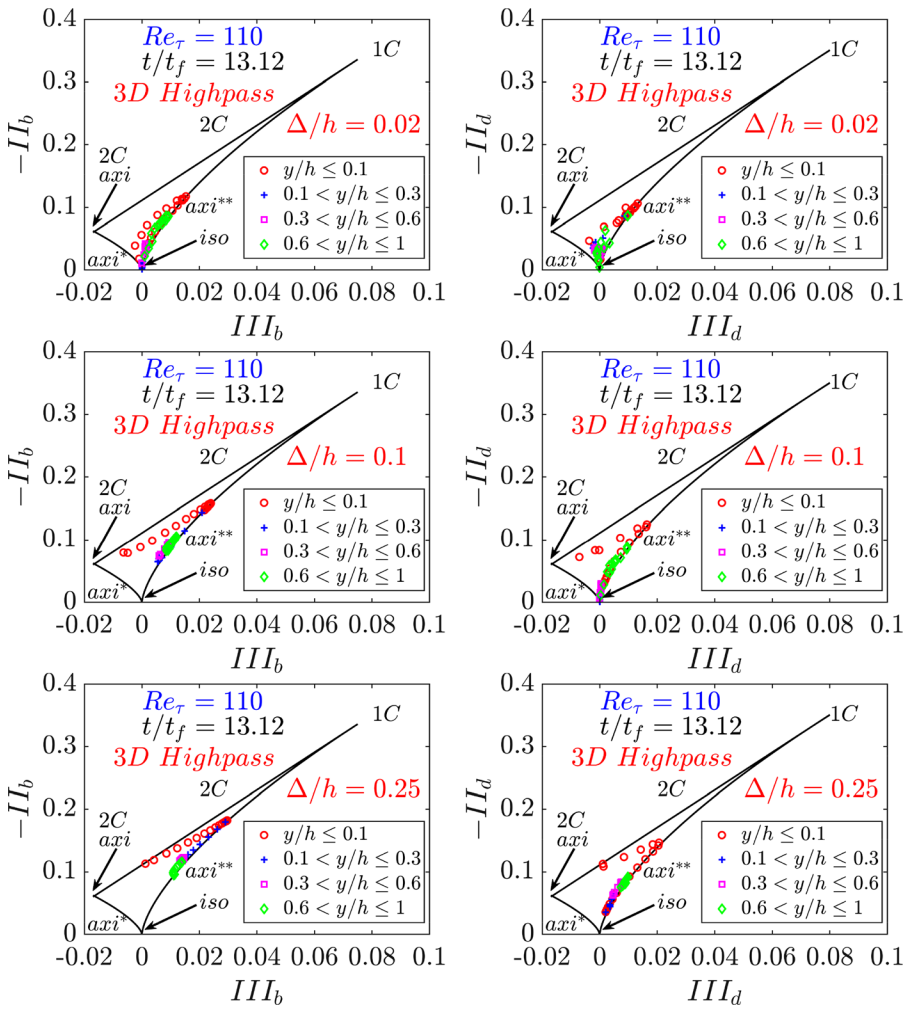

FIG. 16. Plots illustrating $-II_b$ vs III_b for the Reynolds stress tensor (left column) and $-II_d$ vs III_d (right column) for the dissipation rate tensor are represented on the Lumley triangle for 3D high-pass filter with varying filter widths at $t/t_f = 13.12$ for $Re_\tau = 110$.

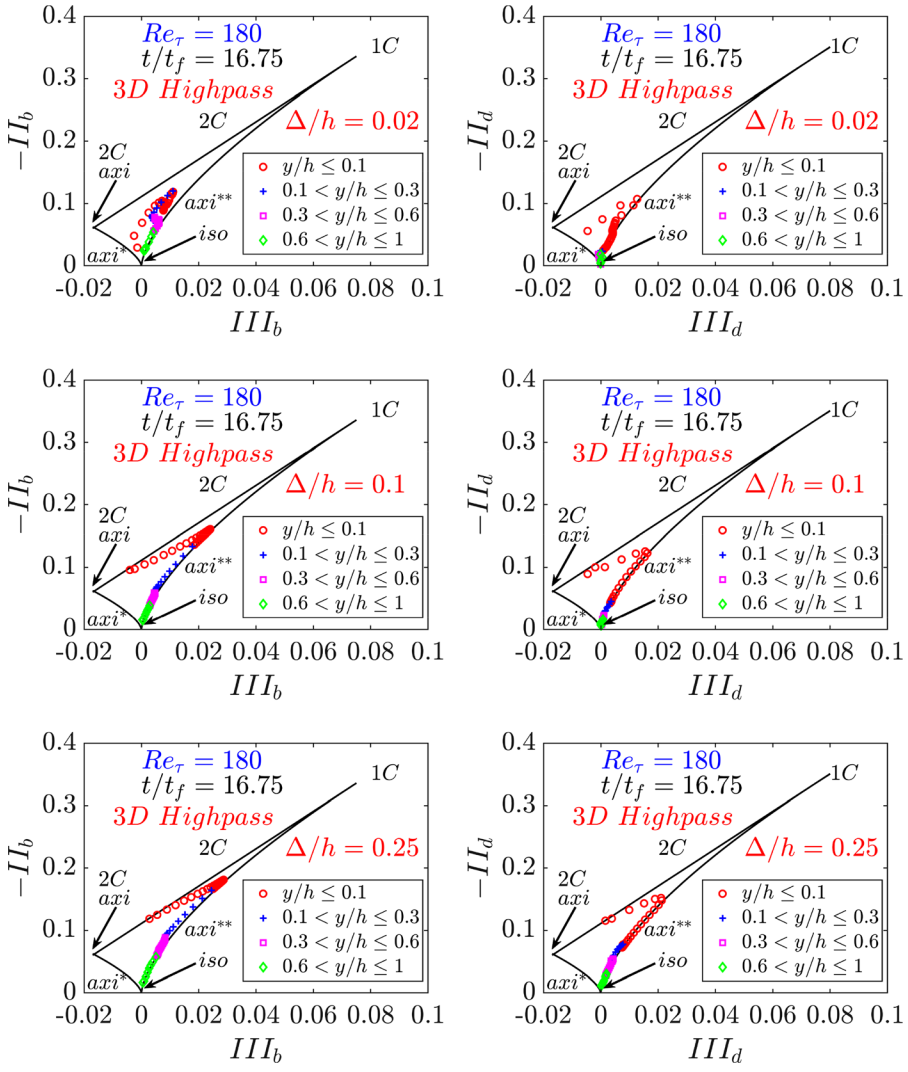

FIG. 17. Plots illustrating $-II_b$ vs III_b for the Reynolds stress tensor (left column) and $-II_d$ vs III_d (right column) for the dissipation rate tensor are represented on the Lumley triangle for 3D high-pass filter with varying filter widths at $t/t_f = 16.75$ for $Re_\tau = 180$.

Upon analyzing the spatial distribution of isotropy at different time instances, specifically at $t/t_f = 3.99$ and 7.89 for $Re_\tau = 110$ and 180, respectively, it becomes apparent that the results obtained from high-pass filtering exhibit maximal isotropy near $y/h \approx 1.0$ when the flame is away from the wall. However, with an increase in the high-pass filter width, a discernible augmentation in isotropy near $y/h \approx 1.0$ is observed especially at early times when the flame is away from the wall. However, the extent of isotropy even at $y/h \approx 1.0$ decreases with the progress of FWI. This observation aligns with the prevailing understanding that smaller filter widths in high-pass filters amplify the influence of small-scale structures, inherently characterized by higher levels of isotropy.

Furthermore, it is noteworthy that at early stages of FWI a tendency toward the 2-component elliptical limit, particularly in proximity to the wall, is evident for high-pass filters with smaller filter widths. However, as the filter width is increased, a transition toward axisymmetric expansion near the wall boundary becomes apparent. This transition underscores the interplay between the scales and the resultant flow characteristics, particularly in regions close to wall boundaries.

V. CONCLUSIONS

Multiscale analysis of anisotropy of Reynolds stresses and viscous dissipation tensors during premixed FWI within turbulent boundary layers has been conducted in this study using DNS datasets for HOQ of premixed flames propagating through turbulent boundary layers, representative of friction Reynolds numbers Re_τ of 110 and 180. The DNS data have been explicitly filtered using 2D or 3D Gaussian filter kernels, to shed light on the complex interplay between turbulence and boundary effects across a range of filter sizes. While both 2D and 3D filtering demonstrate efficacy in predicting trends of Reynolds stress and viscous dissipation tensors, the latter offers a more comprehensive depiction of turbulent flow dynamics. Both 2D and 3D filters yield qualitatively similar trends but there are quantitative differences: Close

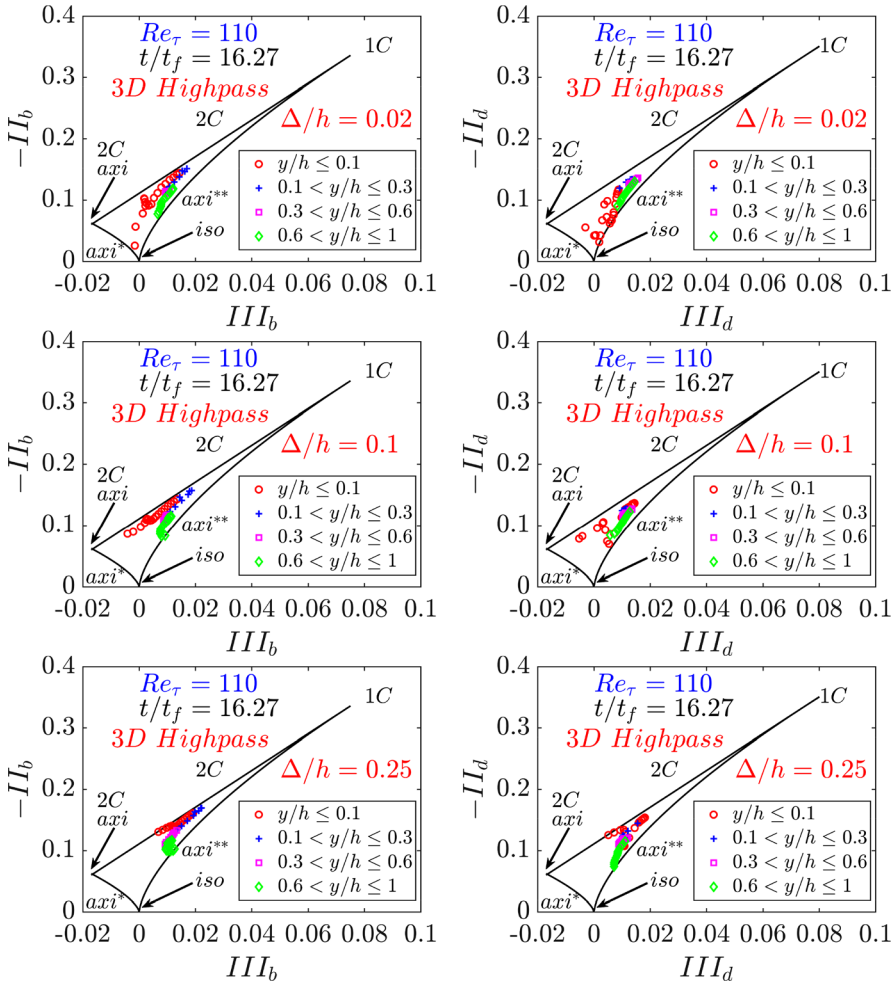

FIG. 18. Plots illustrating $-II_b$ vs III_b for the Reynolds stress tensor (left column) and $-II_d$ vs III_d (right column) for the dissipation rate tensor are represented on the Lumley triangle for 3D high-pass filter with varying filter widths at $t/t_f = 16.27$ for $Re_\tau = 110$.

to the wall, the 2D and 3D filtering operation become similar for the choice of the 3D filter used in this work, whereas away from the wall the 3D filter becomes truly isotropic. The low-pass filtering unveils a transition from a 2-component elliptical limit to a 1-component limit near the wall with increasing filter width, accompanied by diminished isotropy. This signifies the fact that in large eddy simulation (LES) of wall-bounded turbulence, the near-wall flow features need to be resolved (e.g., resolution of viscous sub-layer) to capture the correct flow statistics. The high-pass filtering reveals a progressive increase in anisotropy close to the wall with an increase in filter width, underscoring the pivotal role of filter width in shaping near-wall flow characteristics. Furthermore, qualitative similarities between the behaviors of the second and third invariants of the Reynolds stress tensor and the dissipation rate tensor throughout FWI suggest a link between Reynolds stress and viscous dissipation rate distributions. However, a stronger isotropic behavior in the viscous dissipation rate tensor is observed when the flame is away from the wall, contrasting with a gradual shift toward a 1-component limit as FWI progresses, signifying an increase in anisotropy amidst evolving flow dynamics. In general, the flame induces considerable anisotropy due to flame-normal acceleration caused by thermal expansion and in addition because of Reynolds number effects, as the kinematic viscosity increases on the burned gas side. In addition, the changes in Reynolds stresses suggest considerable modifications to the turbulent boundary layer flow structures. The comparison of both friction Reynolds numbers also confirms the higher levels of isotropy for higher Re_τ. These findings have significant implications for turbulence modeling approaches for FWI, necessitating a detailed consideration of filter size and dimensionality in capturing the interplay between turbulence and boundary layer effects in FWI scenarios.

The paper deals with the multiscale analysis of Reynolds stresses and the filtering operation is used to demonstrate the contributions arising from different scales. Klein *et al.*[5] used multiscale analysis to demonstrate that the anisotropies of sub-grid stress and viscous dissipation rate tensors are qualitatively similar to those for Reynolds stress and viscous dissipation rate tensors in RANS, respectively, for premixed turbulent flames without any influence of walls. A preliminary analysis revealed that the anisotropies of sub-grid stresses and dissipation rate are qualitatively similar to those of Reynolds stresses and its dissipation rates in the FWI configuration analyzed here, but further analysis will be necessary in this regard. Moreover, the turbulent flow statistics for the fully developed channel flow boundary layer for

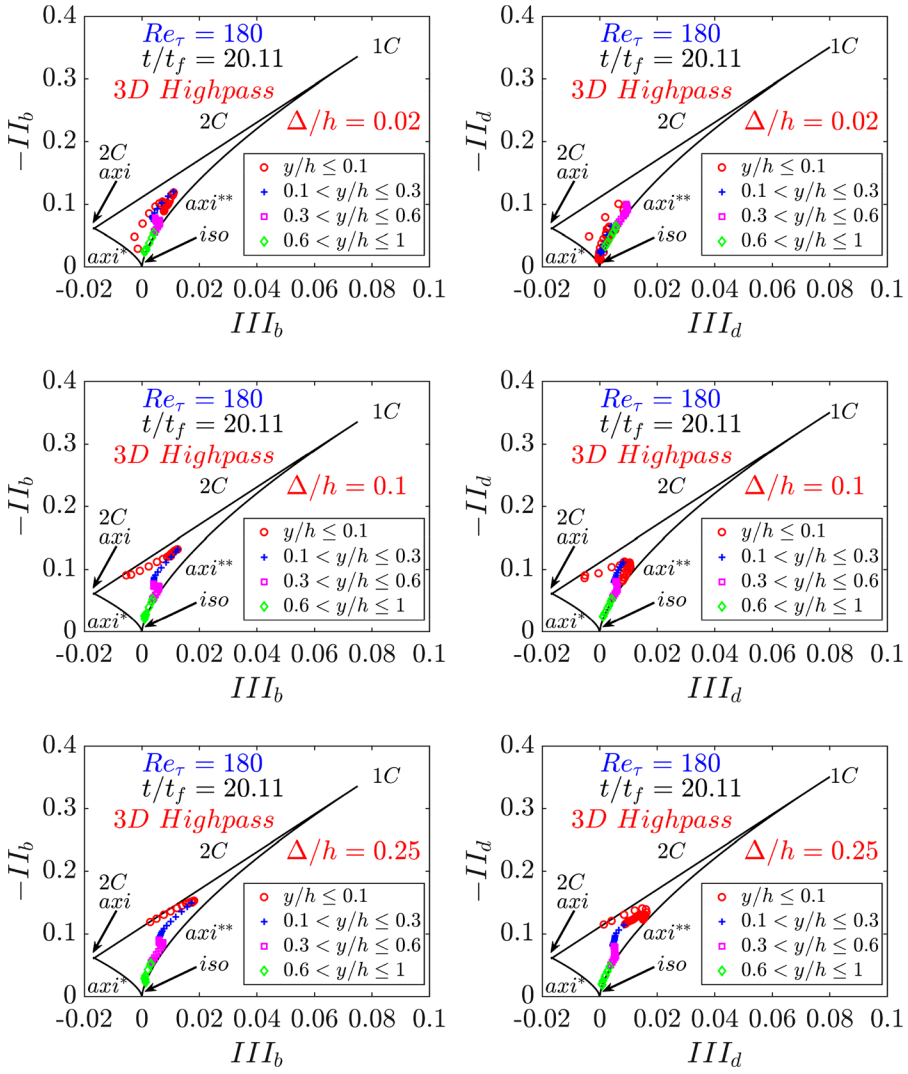

FIG. 19. Plots illustrating $-II_b$ vs III_b for the Reynolds stress tensor (left column) and $-II_d$ vs III_d (right column) for the dissipation rate tensor are represented on the Lumley triangle for 3D high-pass filter with varying filter widths at $t/t_f = 20.11$ for $Re_\tau = 180$.

$Re_\tau = 180$ are qualitatively similar to those for the channel flow cases with higher Re_τ (Ref. 31) and thus it can be expected that the results obtained in this analysis are likely to be qualitatively valid for higher values of Reynolds number. Moreover, it was demonstrated by Ahmed *et al.*[47] that the anisotropy statistics of the Reynolds stress tensor for both isothermal and adiabatic wall boundary conditions are qualitatively and mostly quantitatively similar. Thus, the sensitivity of the anisotropy results on the thermal boundary condition is not addressed in this paper. However, this needs to be confirmed by further analyses in the presence of detailed chemistry and transport for different thermal boundary conditions at higher values of Reynolds number.

ACKNOWLEDGMENTS

The authors are grateful for the financial and computational supports from the Engineering and Physical Sciences Research Council (Grants EP/V003534/1 and EP/R029369/1), ARCHER2 Pioneer Projects (e691 and e817), CIRRUS, and ROCKET HPC facility.

AUTHOR DECLARATIONS

Conflict of Interest

The authors have no conflicts to disclose.

Author Contributions

Sanjeev Ghai: Formal analysis (lead); Writing – original draft (lead); Software (lead); Conceptualization (equal); Methodology (equal); Data curation (supporting); Visualization (equal); Writing – review & editing (equal). **Umair Ahmed:** Conceptualization (supporting); Data curation (lead); Methodology (equal); Supervision (equal); Writing – review & editing (equal); Funding acquisition (supporting). **Nilanjan**

Chakraborty: Conceptualization (lead); Methodology (equal); Supervision (equal); Writing – original draft (supporting); Funding acquisition (lead); **Markus Klein:** Conceptualization (lead); Methodology (equal); Supervision (equal); Writing – original draft (supporting).

DATA AVAILABILITY

The data that support the findings of this study are available from the corresponding author upon reasonable request.

REFERENCES

[1]T. Alshaalan and C. J. Rutland, "Wall heat flux in turbulent premixed reacting flow," Combust. Sci. Technol. **174**, 135 (2002).
[2]A. Gruber, R. Sankaran, E. R. Hawkes, and J. H. Chen, "Turbulent flame-wall interaction: A direct numerical simulation study," J. Fluid Mech. **658**, 5 (2010).
[3]A. N. Kolmogorov, V. Levin, J. C. R. Hunt, O. M. Phillips, and D. Williams, "The local structure of turbulence in incompressible viscous fluid for very large Reynolds numbers," Proc. R. Soc. Lond. **A434**, 9–13 (1991).
[4]S. B. Pope, *Turbulent Flows*, 1st ed. (Cambridge University Press, 2000).
[5]M. Klein, T. Trummler, N. Urban, and N. Chakraborty, "Multiscale analysis of anisotropy of Reynolds Stresses, subgrid stresses and dissipation in statistically planar turbulent premixed flames," Appl. Sci. **12**, 2275 (2022).
[6]K. R. Sreenivasan and R. A. Antonia, "The phenomenology of small-scale turbulence," Annu. Rev. Fluid Mech. **29**, 435 (1997).
[7]X. Shen and Z. Warhaft, "The anisotropy of the small scale structure in high Reynolds number ($R\lambda \sim 1000$) turbulent shear flow," Phys. Fluids **12**, 2976 (2000).
[8]K. Liu and R. H. Pletcher, "Anisotropy of a turbulent boundary layer," J. Turbul. **9**, N18 (2008).
[9]M. Klein, T. Trummler, and J. Radtke, "Multiscale analysis of the Reynolds stress, dissipation, and subgrid-scale tensor in turbulent bubbly channel flows: Characterization of anisotropy and modeling implications," Phys. Fluids **34**, 085122 (2022).
[10]M. Holzner, J. Jiménez, and A. Lozano-Durán, "Multiscale analysis of the topological invariants in the logarithmic region of turbulent channels at a friction Reynolds number of 932," J. Fluid Mech. **803**, 356 (2016).
[11]U. Ahmed, N. A. K. Doan, J. W. Lai, M. Klein, N. Chakraborty, and N. Swaminathan, "Multiscale analysis of head-on quenching premixed turbulent flames," Phys. Fluids **30**, 105102 (2018).
[12]K. W. Jenkins and R. S. Cant, *Direct Numerical Simulation of Turbulent Flame Kernels* (Springer Netherlands, Dordrecht, 1999).
[13]E. F. Tarrazo, A. L. Sánchez, A. Linan, and F. A. Williams, "A simple one-step chemistry model for partially premixed hydrocarbon combustion," Combust. Flame **147**, 32–38 (2006).
[14]S. P. Malkeson and N. Chakraborty, "A priori direct numerical simulation analysis of algebraic models of variances and scalar dissipation rates for Reynolds averaged Navier Stokes simulations for low Damköhler number turbulent partially-premixed combustion," Combust. Sci. Technol. **182**, 960–999 (2010).
[15]M. D. Smooke and V. Giovangigli, *Premixed and Nonpremixed Test Problem Results* (Springer, Berlin, Heidelberg, 1991), pp. 29–47.
[16]T. J. Poinsot, D. Haworth, and G. Bruneaux, "Direct simulation and modeling of flame-wall interaction for premixed turbulent combustion," Combust. Flame **95**(1), 118–132 (1993).
[17]J. Lai and N. Chakraborty, "Effects of Lewis number on head on quenching of turbulent premixed flame: A direct numerical simulation analysis," Flow Turbul. Combust. **96**, 279–308 (2016).
[18]J. Sellmann, J. Lai, A. M. Kempf, and N. Chakraborty, "Flame surface density based modelling of head-on quenching of turbulent premixed flames," Proc. Combust. Inst. **36**(2), 1817–1825 (2017).
[19]G. Bruneaux, K. Akselvol, J. H. Ferziger, and T. Poinsot, "Flame-wall interaction simulation in a turbulent channel flow," Combust. Flame **107**(1–2), 27–36 (1996).
[20]T. Alshaalan and C. J. Rutland, "Turbulence, scalar transport, and reaction rates in flame-wall interaction," Proc. Combust. Inst. **27**(1), 793–799 (1998).
[21]J. Lai, M. Klein, and N. Chakraborty, "Direct numerical simulation of head-on quenching of statistically planar turbulent premixed methane-air flames using a detailed chemical mechanism," Flow Turbul. Combust. **101**, 1073 (2018).
[22]J. Lai, U. Ahmed, M. Klein, and N. Chakraborty, "A comparison between head-on quenching of stoichiometric methane-air and hydrogen-air premixed flames using direct numerical simulations," Int. J. Heat Fluid Flow **93**, 108896 (2022).
[23]S. R. Vosen, R. Greif, and C. K. Westbrook, "Unsteady heat transfer during laminar flame quenching," Proc. Combust. Inst. **20**(1), 75–83 (1985).
[24]J. Jarosinski, "A survey of recent studies on flame extinction," Prog. Energy Combust. Sci. **12**(2), 81–116 (1986).
[25]W. M. Huang, S. R. Vosen, and R. Greif, "Heat transfer during laminar flame quenching: Effect of fuels," Proc. Combust. Inst. **21**(1), 1853–1860 (1988).
[26]D. Zhao, C. Zhang, F. E. Hernández Pérez, H. G. Im, and L. Wang, "Turbulent premixed hydrogen/air flame-wall interaction with heterogeneous surface reactions," Proc. Combust. Inst. **39**, 2189–2197 (2023).
[27]A. Gruber, J. H. Chen, D. Valiev, and C. K. Law, "Direct numerical simulation of premixed flame boundary layer flashback in turbulent channel flow," J. Fluid Mech. **709**, 516–542 (2012).
[28]T. Kitano, T. Tsuji, R. Kurose, and S. Komori, "Effect of pressure oscillations on flashback characteristics in a turbulent channel flow," Energy Fuels **29**(10), 6815–6822 (2015).
[29]U. Ahmed, N. Chakraborty, and M. Klein, "Influence of thermal wall boundary condition on scalar statistics during flame-wall interaction of premixed combustion in turbulent boundary layers," Int. J. Heat Fluid Flow **92**, 108881 (2021b).
[30]S. K. Ghai, U. Ahmed, M. Klein, and N. Chakraborty, "Turbulent kinetic energy evolution in turbulent boundary layers during head-on interaction of premixed flames with inert walls for different thermal boundary conditions," Proc. Combust. Inst. **39**, 2169 (2023).
[31]T. Tsukahara, Y. Seki, H. Kawamura, and D. Tochio, "DNS of turbulent channel flow at very low Reynolds numbers," in *Proceedings of the 4th International Symposium on Turbulence and Shear Flow Phenomena*, 2005, p. 935.
[32]S. K. Ghai, N. Chakraborty, U. Ahmed, and M. Klein, "Enstrophy evolution during head-on wall interaction of premixed flames within turbulent boundary layers," Phys. Fluids **34**(7), 075124 (2022).
[33]J. J. Gorski, J. M. Wallace, and P. M. Bernard, "The enstrophy equation budget of bounded turbulent shear flows," Phys. Fluids **6**, 3197 (1994).
[34]R. Kai, A. L. Pillai, U. Ahmed, N. Chakraborty, and R. Kurose, "Analysis of the evolution of the surface density function during premixed V-shaped flame-wall interaction in a turbulent channel flow at $Re_\tau = 395$," Combust. Sci. Technol. (published online 2022).
[35]F. Zentgraf, P. Johe, M. Steinhausen, C. Hasse, M. Greifenstein, A. D. Cutler, R. S. Barlow, and A. Dreizler, "Detailed assessment of the thermochemistry in a side-wall quenching burner by simultaneous quantitative measurement of CO_2, CO and temperature using laser diagnostics," Combust. Flame **235**, 111707 (2022).
[36]F. Zentgraf, P. Johe, A. D. Cutler, R. S. Barlow, B. Böhm, and A. Dreizler, "Classification of flame prehistory and quenching topology in a side-wall quenching burner at low-intensity turbulence by correlating transport effects with CO_2, CO and temperature," Combust. Flame **239**, 111681 (2022).
[37]F. Zentgraf, P. Johe, A. Nicolas, R. S. Barlow, B. Böhm, B. Peterson, and A. Dreizler, "On the evolution of turbulent boundary layers during flame–wall interaction investigated by highly resolved laser diagnostics," Combust. Flame **261**, 113276 (2024).
[38]R. D. Moser, J. Kim, and N. N. Mansour, "Direct numerical simulation of turbulent channel flow up to $Re_\tau = 590$," Phys. Fluids **11**, 943 (1999).
[39]U. Ahmed, N. Chakraborty, and M. Klein, "Assessment of Bray Moss Libby formulation for premixed flame-wall interaction within turbulent boundary layers: Influence of flow configuration," Combust. Flame **233**, 111575 (2021).
[40]U. Ahmed, N. Chakraborty, and M. Klein, "Scalar gradient and strain rate statistics in oblique premixed flame-wall interaction within turbulent channel flows," Flow Turbul. Combust. **106**, 701 (2021).
[41]U. Ahmed, D. Apsley, T. Stallard, P. Stansby, and I. Afgan, "Turbulent length scales and budgets of Reynolds stress-transport for open-channel flows; friction Reynolds numbers $Re_\tau = 150$, 400 and 1020," J. Hydraul. Res. **59**, 36 (2021a).
[42]N. Peters, *Turbulent Combustion* (Cambridge University Press, Cambridge, 2010).

[43]C. S. Yoo and H. G. Im, "Characteristic boundary conditions for simulations of compressible reacting flows with multi-dimensional, viscous and reaction effects," Combust. Theor. Model. **11**, 259 (2007).
[44]D. C. Wilcox, *Turbulence Modeling for CFD*, 2nd ed. (DCW Industries, 1998).
[45]R. A. Antonia, L. Djenidi, and P. R. Spalart, "Anisotropy of the dissipation tensor in a turbulent boundary layer," Phys. Fluids **6**, 2475 (1994).
[46]J. L. Lumley and G. R. Newman, "The return to isotropy of homogeneous turbulence," J. Fluid Mech. **82**, 161 (1977).
[47]U. Ahmed, N. Chakraborty, and M. Klein, "Influence of flow configuration and thermal wall boundary conditions on turbulence during premixed flame-wall interaction within low Reynolds number boundary layers," Flow Turbul. Combust. **111**, 825–866 (2023).